

1 SEARCH FOR STANDARD MODEL TOP QUARK AND Z BOSON ASSOCIATED
2 PRODUCTION AT ATLAS

3 By

4 Brad Schoenrock

5 A DISSERTATION

6 Submitted to
7 Michigan State University
8 in partial fulfillment of the requirements
9 for the degree of

10 Physics - Doctor of Philosophy

11 2016

ABSTRACT

SEARCH FOR STANDARD MODEL TOP QUARK AND Z BOSON ASSOCIATED PRODUCTION AT ATLAS

By

Brad Schoenrock

This document reports the measurement of the top-quark Z -boson associated production cross-section using data from the ATLAS detector. The data used were collected during 2015, from proton-proton collisions with a 13 TeV center-of-mass collision energy. To isolate this production, selections are applied to find events with a specific final state. A cut-based analysis is used to isolate tZ using a series of selections in several kinematic regions. A statistical analysis is performed to determine the measured cross-section and check that the measured value with the standard model prediction. The resulting cross-section measurement is $\sigma_{tZ} = XYZ \pm abc$.

25 —changelog—

26 June 22, 2016

27 Figures 1.7 and 1.8 updated font sizes.

²⁸ line 912: this seems to repeat the beginning of section 6.3 -

ACKNOWLEDGMENTS

TABLE OF CONTENTS

30	LIST OF TABLES	vii
31	LIST OF FIGURES	viii
32	Chapter 1 Introduction	1
33	1.1 The Standard Model	1
34	1.2 Feynman Diagrams	5
35	1.3 Top-Quark Physics	7
36	1.4 tZ Associated Production	9
37	Chapter 2 CERN, the LHC, and ATLAS	14
38	2.1 The Accelerator Chain	14
39	2.2 The Large Hadron Collider	15
40	2.3 ATLAS	20
41	2.3.1 Magnet System	24
42	2.3.2 Inner Detector	26
43	2.3.3 Calorimeters	31
44	2.3.4 Muon Systems	33
45	Chapter 3 The Trigger System on ATLAS	37
46	3.1 Level 1 Trigger	39
47	3.2 High Level Trigger	40
48	3.3 Trigger Chains	41
49	3.3.1 Single Muon	42
50	3.3.2 Single Electron	43
51	Chapter 4 Event Simulation	44
52	4.1 The Monte Carlo Method	44
53	4.2 Signal Simulation	45
54	4.3 Diboson	45
55	4.4 $t\bar{t}$	45
56	4.5 $t\bar{t}+X$	46
57	4.6 Z -boson+jets	46
58	4.7 Single top-quark	46
59	4.8 W -boson+jets and Multijet	47
60	Chapter 5 Object & Event Reconstruction	48
61	5.1 Electron Reconstruction	48
62	5.2 Muon Reconstruction	49

63	5.3 Jet Reconstruction	50
64	5.3.1 Jet <i>b</i> -tagging	51
65	5.4 <i>Z</i> boson	52
66	5.5 Missing Transverse Energy and the <i>W</i> -boson	52
67	5.6 Reconstructing the top-quark	54
68	Chapter 6 Analysis	55
69	6.1 Preselection	55
70	6.2 Control Regions	56
71	6.3 Cut Flow	56
72	Chapter 7 Results	65
73	7.1 Systematic Uncertainties	65
74	7.2 Statistical Analysis	65
75	7.3 Conclusions	65
76	7.4 more citations	65
77	BIBLIOGRAPHY	67

LIST OF TABLES

LIST OF FIGURES

81	Figure 1.1	The SM of high energy physics.	2
82	Figure 1.2	History of high energy physics illustrating the time it took from theorizing the existence of the particles until discovery [3].	3
84	Figure 1.3	Feynman diagram for the t -channel single top-quark process [4].	8
85	Figure 1.4	Feynman diagrams for the Wt -channel single top-quark process [4].	8
86	Figure 1.5	Feynman diagram for the s -channel single top-quark process [4].	8
87	Figure 1.6	Feynman diagram for the tZ associated production going to three leptons [5].	10
89	Figure 1.7	Truth information drawn from Madgraph simulation of tZ . Light jet p_T and η as well as b-quark p_T and η .	11
91	Figure 1.8	Truth information drawn from Madgraph simulation of tZ . The p_T of other objects in tZ .	12
93	Figure 1.9	Top-Quark pair and single top-quark cross-sections with and without accompanying Z boson [6].	13
95	Figure 2.1	Diagram of the accelerator complex for protons to get to the LHC [7].	16
96	Figure 2.2	A Segment of the LHC beampipe [8].	17
97	Figure 2.3	Peak instantaneous luminosity over time. As run 2 went on instantaneous luminosity was increased to maximize data collection showing the dramatic increase in data collection in August and September [9].	18
100	Figure 2.4	Total LHC delivered integrated luminosity over time for run 1 [9]	19
101	Figure 2.5	Total LHC delivered integrated luminosity over time for run 2 [9]	19

102	Figure 2.6	Number of interactions per crossing is a measure of in time pile up. This is comparing the number of interactions per crossing in the LHC 7 TeV run and the 8 TeV run [9].	20
103			
104			
105	Figure 2.7	Number of interactions per crossing is a measure of in time pile up. This figure is for run 2 which is in comparison to Figure 2.6 which is for run 1 [9].	20
106			
107			
108	Figure 2.8	ATLAS with its namesake toroidal magnets prominently visible [10].	21
109			
110	Figure 2.9	A figure diagramming how particle identification can be achieved us- ing multiple layers of the detector [11].	23
111			
112	Figure 2.10	Cutaway diagram of ATLAS [12].	24
113			
114	Figure 2.11	Illustration of the ATLAS magnet system, showing the barrel solenoid, barrel toroid, and endcap toroid coils [13].	25
115			
116	Figure 2.12	A mapping of the magnetic fields in atlas. Note the inhomogeneous nature of the toroidal field and the comparative constant nature of the solenoidal field [14].	25
117			
118	Figure 2.13	Preparation for lowering an endcap magnet into the ATLAS cav- ern [15].	27
119			
120	Figure 2.14	Cutaway diagram of the ATLAS inner detector [16].	28
121			
122	Figure 2.15	A diagram of the sub detectors of the inner detector with relative radial positions [13]	29
123			
124	Figure 2.16	Cutaway diagram of the ATLAS calorimeter systems [17].	32
125			
126	Figure 2.17	Cutaway diagram of the ATLAS muon spectrometer and toroid mag- net systems [18].	34
127			
128	Figure 2.18	The TGC wheel [19].	36
129			
130	Figure 3.1	A Z -boson decaying to an electron positron pair.	38
131			
132	Figure 6.1	Lepton p_T for leading (a), second (b), and third (c) leptons with preselection applied except the cuts on the variable shown.	57
133			

129	Figure 6.2	Number of jets (a), number of b-jets (b), and p_T of the leading jet (c) with preselection applied except the cuts on the variable shown. At least one jet was required at this level.	58
132	Figure 6.3	Further histograms with preselection applied except the cuts on the variable shown. Invariant mass of the Z -boson (c), two dimensional map of transverse mass of the W -boson vs MET for the signal (a), and two dimensional map of transverse mass of the W -boson vs MET for the data (b).	59
137	Figure 6.4	Variables with full selection applied except the cut on this variable.	61
138	Figure 6.5	Lepton p_T for leading, second, and third leptons with full selection applied as well as histograms of the three cuts made to finalize selection with full selection applied.	62
141	Figure 6.6	Number of jets with full selection applied.	63
142	Figure 6.7	Leading Jet Pt with full selection applied.	63
143	Figure 6.8	Histograms of number of electrons. Note that because we require three leptons exactly these histograms are mirrors of each other by definition.	63
146	Figure 6.9	Histograms of number of muons. Note that because we require three leptons exactly these histograms are mirrors of each other by definition.	63
149	Figure 6.10	Variables which display properties of the top quark and its decay with full selection applied.	64

¹⁵¹ **Chapter 1**

¹⁵² **Introduction**

¹⁵³ High energy physics is concerned with obtaining the most fundamental understanding of the
¹⁵⁴ universe. In practice this means categorizing all fundamental particles and their interactions
¹⁵⁵ in order to understand what the world is made of. Assorted scientific fields question what
¹⁵⁶ the world is made of in various detail. Chemistry asks which atoms and molecules comprise
¹⁵⁷ the things around us, nuclear physics investigates what makes up atoms and how atoms
¹⁵⁸ are formed, and high energy physics is studying what we currently think are the most
¹⁵⁹ fundamental particles in existence. In order to understand high energy physics we need a
¹⁶⁰ mathematical framework to describe the elementary particles and their interactions. This
¹⁶¹ framework is referred to as the Standard Model (SM).

¹⁶² **1.1 The Standard Model**

¹⁶³ The SM of high energy physics has been among the most successful theories of the past
¹⁶⁴ century. It has been tested again and again and has encountered few unexplained anomalies.
¹⁶⁵ It started as an effort to combine the fundamental forces we know into one overarching theory.
¹⁶⁶ Electricity and magnetism had been combined into electromagnetism long ago and in the
¹⁶⁷ last century the SM was developed. Electromagnetism was combined with weak interactions,
¹⁶⁸ followed by the inclusion of the Higgs mechanism and strong interactions to form the SM we
¹⁶⁹ know today [20, 21, 22].

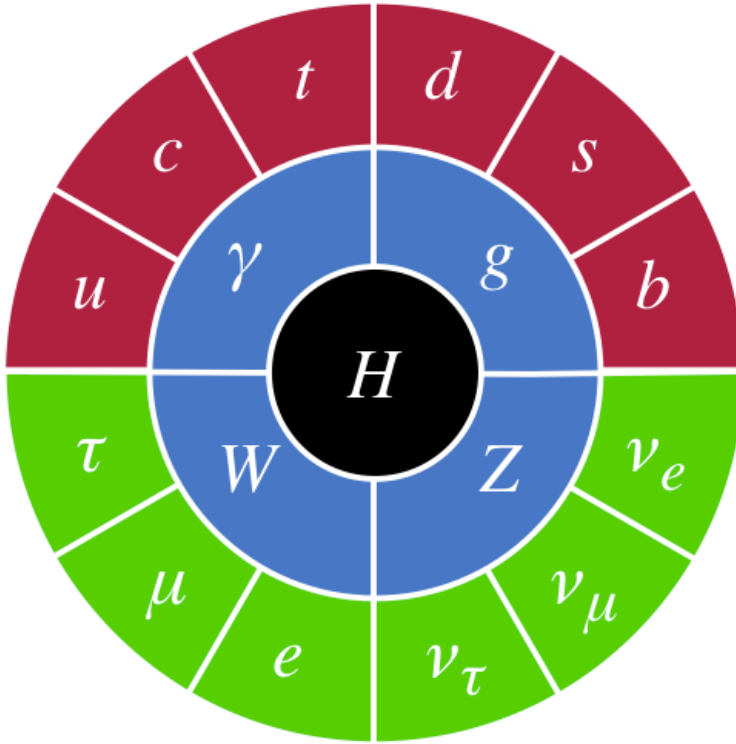


Figure 1.1: The SM of high energy physics.

170 The SM particles we have found are classified based on their properties and interactions
 171 and shown in Figure 1.1. One way we can classify particles is by their spin. A particle
 172 with half integer spin is called a fermion while a particle with integer spin is a boson. All
 173 discovered fundamental particles are either spin 0, spin $\frac{1}{2}$ or spin 1. We further break
 174 down the fermions into two categories, the first set are the leptons which can be charged
 175 (electron, muon, and tau) to interact with the electroweak force, and three neutral neutrinos
 176 which only interact via the weak force. The other type of fermion is the quark. Quarks
 177 interact via the weak, electromagnetic, and strong forces. The strong force, at low energies,
 178 imparts color confinement onto individual quarks which binds them together in mesons
 179 (quark antiquark pairs) or baryons (three quark systems such as the proton or neutron).
 180 Quarks also interact electromagnetically and weakly like their charged leptonic counterparts.
 181 The vector bosons (spin 1) moderate the forces involved in the Standard Model. The gluon

182 interacts via the strong force, the photon interacts electromagnetically, and the W^\pm and
 183 Z bosons only interact weakly. The final particle we have is the recently discovered Higgs
 184 boson which took nearly 50 years to discover. A history of particle discovery can be seen in
 185 Figure 1.2 [23].

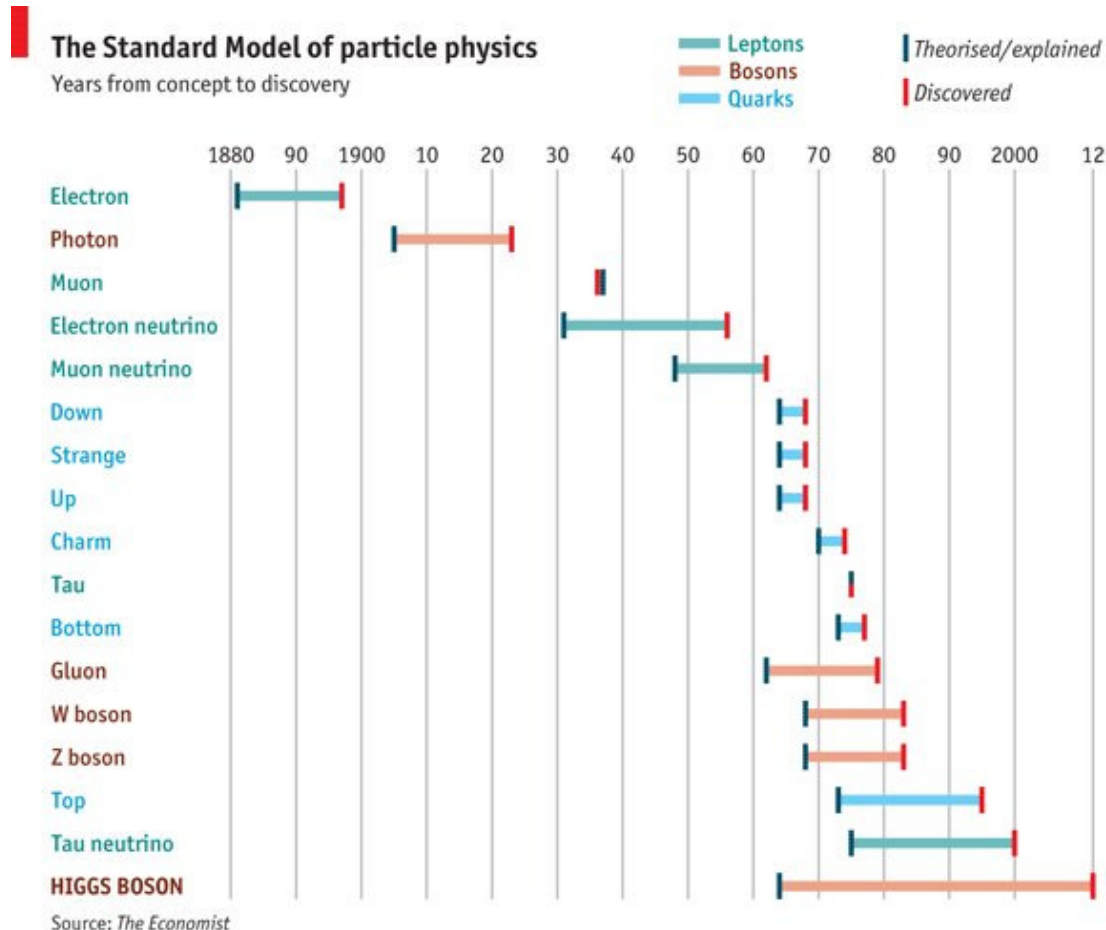


Figure 1.2: History of high energy physics illustrating the time it took from theorizing the existence of the particles until discovery [3].

186 A deeper understanding of the SM can be obtained through the Lagrange density [21]

$$\begin{aligned}\mathcal{L} = & -\frac{1}{2} \text{tr}[G_{\mu\nu}G^{\mu\nu}] - \frac{1}{4}F_{\mu\nu}F^{\mu\nu} - \frac{1}{2\xi}(\delta^\mu A_\mu)^2 \\ & + i\bar{\psi}[\not{D} - m]\psi + \psi_i y_{ij} \psi_j \phi + h.c. + |D_\mu \phi|^2 - V(\phi)\end{aligned}\quad (1.1)$$

187 Where ψ is the Dirac field, A_μ is the electromagnetic potential, ξ represents a gauge
 188 fixing choice, ($\xi=0$ is Landau gauge, while $\xi=1$ is Feynman gauge), ϕ is the Higgs field, y_{ij}
 189 are the Yukawa couplings, \not{D} is defined through Dirac slash notation as

$$\not{D} = \gamma_\mu D^\mu \quad (1.2)$$

$$D^\mu = \delta^\mu - ieA^\mu \quad (1.3)$$

190 $F_{\mu\nu}$ is the electromagnetic field tensor defined as

$$F_{\mu\nu} = \delta_\mu A_\nu - \delta_\nu A_\mu = \begin{pmatrix} 0 & -E_x & -E_y & -E_z \\ E_x & 0 & -B_z & B_y \\ E_y & B_z & 0 & -B_x \\ E_z & -B_y & B_x & 0 \end{pmatrix} \quad (1.4)$$

191 and $G_{\mu\nu}$ is the QCD field tensor defined as

$$G_{\mu\nu} = \frac{\lambda_a}{2} G_{\mu\nu}^a = \frac{i}{g} [D_\mu, D_\nu] \quad (1.5)$$

$$G_{\mu\nu}^a = \delta_\mu A_\nu^a - \delta_\nu A_\mu^a + g f^{abc} A_{\mu b} A_{\nu c} \quad (1.6)$$

192 The SM Lagrangian in equation 1.1 contains a lot of information on the SM in one

193 concise equation. The first three terms in the Lagrange density formula contains the strong
194 and electroweak forces, the fourth term describes how the particles interact with these fields,
195 the fifth term and its Hermetian conjugate(*h.c.*) describes how the fermions get their masses
196 (note the ϕ dependence means that the Higgs contributes but does not define their masses),
197 the next to last term describe how the Higgs gives mass to the bosons, and the final term is
198 the Higgs potential [20, 21, 22].

199 This formulation represents a group with a $SU(3) \times SU(2) \times U(1)$ symmetry. The $SU(3)$
200 represents the strong force, with the threefold symmetry in color charge. Every group G
201 has a set of generators S which is the smallest subset of G through which the combinations
202 of these generators and their inverses can recover every element of G . The eight generators
203 of this $SU(3)$ symmetry correspond to the various color combinations of the gluon which
204 can be mathematically represented by the Gell-Mann matrices. While no independent weak
205 theory has been formulated to date, the $SU(2) \times U(1)$ represents the electroweak force which
206 unified electricity, magnetism, and the weak forces whose generators can be represented by
207 the Pauli matrices. The Higgs mechanism breaks this symmetry and this phenomenon is
208 known as electroweak symmetry breaking. The broken combination of the $SU(2) \times U(1)$
209 symmetry has the massive W^+ , W^- , and Z^0 bosons while the unbroken $U(1)$ has the
210 massless photon [24, 25].

211 1.2 Feynman Diagrams

212 Thanks to Richard Feynman we can obtain an intuitive understanding of particles and
213 their interactions through Feynman diagrams. We can view these pictures as having direct
214 correlation with the processes involved and even set up the relevant equations to compute

215 their contributions to the overall cross-section. In these diagrams we compact the spacial
216 dimensions into one vertical axis while time is represented on the horizontal axis.

217 The cross-section for a particular process is defined as the ratio of number of particles
218 scattered in a certain way per unit time ($dN(t)$) to number of particles passing through a
219 defined area per unit time (n), see equation 1.7.

$$d\sigma(t) = dN(t)/n \quad (1.7)$$

$$N_{events} = \sigma \int L(t) dt \quad (1.8)$$

$$L(t) = f * \frac{n_1 n_2}{4\pi\sigma_x\sigma_y} \quad (1.9)$$

220 Informally this is how probable that process is to be created in each interaction. The
221 standard unit for cross-section is the Barn (10^{-24} cm^2) but we commonly use picobarn
222 or femtobarn to describe cross-sections. Consequently we define the beam intensity, or
223 luminosity (L), in inverse picobarns or inverse femtobarns. That way we can easily calculate
224 the expected number of events by equation 1.8. Luminosity can be calculated from the
225 beam parameters of the accelerator by equation 1.9 where n_1 and n_2 are the number of
226 particles in each beam, and σ_x and σ_y are the Gaussian RMS beam sizes in their respective
227 directions. [21]

228 1.3 Top-Quark Physics

229 The top-quark is of specific interest to this field and in particular this thesis. It has a mass
230 that makes it the heaviest fundamental particle that we know of today, $173.21 \pm 0.51 \pm$
231 0.71GeV , which is heavier than most atoms [26].

232 Due to the top-quark's large natural width (defined as the probability per unit time that
233 a particle decays) it is the only quark with an observed decay lifetime (10^{-25} s) shorter than
234 the strong timescale (10^{-24} s) [27, 28, 29].

$$\tau_t = \frac{\hbar}{\Gamma_t} \quad (1.10)$$

$$\Gamma_t = -\frac{1}{N} \frac{dN}{dt} \quad (1.11)$$

235 Because of this, and the fact that the CKM matrix element V_{tb} (V_{tb} corresponds to the
236 strength of the top-quark flavor changing to bottom quark through a weak decay) is approx-
237 imately equal to 1, the top-quark almost always decays into a W -boson and a b -quark before
238 it hadronizes into a jet [30] [21].

239 The top-quark was originally discovered through pair production at the Tevatron in
240 1995 [31], [32]. Later the production of a single top-quark was discovered at the Teva-
241 tron [33] [34] and its width measured [28] [29] [35]. These production channels have also
242 been investigated at the LHC [36].

243 There are three channels of single top-quark physics that have been studied at the
244 LHC. They are t -channel, s -channel, and associated production (also referred to as Wt -
245 channel). The largest contribution to single top is t -channel, followed by Wt -channel, with

246 s -channel being the smallest of the three. Being the largest, t -channel was observed first and
 247 has been observed independently [37]. Evidence of Wt -channel has also been achieved in
 248 ATLAS [38]. Cross-sections for the different single top-quark processes at a pp collider with
 249 $\sqrt{s} = 8 \text{ TeV}$ are given in Table 1.3. \sqrt{s} is the center of mass energy of the proton-proton
 250 collision. At the LHC high energies make gluons in the proton more prevalent when com-
 251 pared to energetic quarks so a look into the initial states of these processes in figures 1.3, 1.4,
 252 and 1.5 reveal the hierarchical nature of their cross-sections.

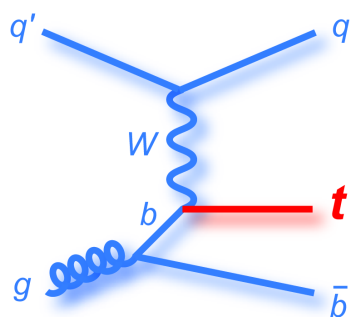


Figure 1.3: Feynman diagram for the t -channel single top-quark process [4].

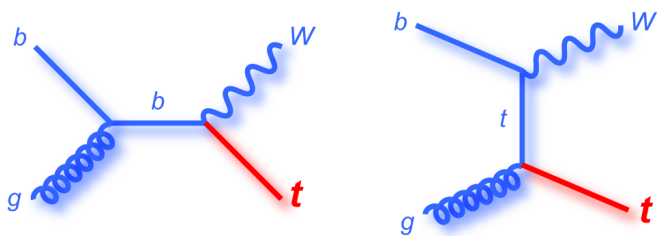


Figure 1.4: Feynman diagrams for the Wt -channel single top-quark process [4].

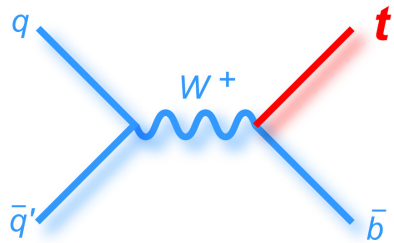


Figure 1.5: Feynman diagram for the s -channel single top-quark process [4].

253 t -channel has an initial state of an energetic gluon as well as a light quark, Wt -channel has
 254 an initial state of an energetic gluon as well as an energetic b-quark (which will be harder
 255 to get from a proton when compared to a light quark which is naturally in a proton), and
 256 s -channel has an energetic antiquark in its initial state making it difficult to produce at the
 257 LHC. While small at the LHC s -channel was not so disfavored at the Tevatron due to the
 258 fact that it was a proton anti-proton collider, making energetic anti-quarks more prevalent.

t -channel	$216.99 +9.04 -7.71$ pb
Wt -channel	$84.4 +5.00 -6.80$ pb
s -channel	$10.32 +0.40 -0.36$ pb

Table 1.1: The cross-section for the production for the different modes of single top-quark production at the LHC at $\sqrt{s} = 8$ TeV [1] [2]

259 1.4 tZ Associated Production

260 The production of a top-quark in association with a Z boson has been, until now, uncon-
 261 sidered at the LHC. The Feynman diagram for tZ can be seen in Figure 1.6. The related
 262 $t\bar{t}Z$ cross section has been able to be measured and although the uncertainty is quite high
 263 the top-quark+ Z -boson processes are a potentially fruitful process to investigate ???. The
 264 competitive rate of the tZ process suggests that it should be visible in the 8 TeV data set as
 265 seen in Figure 1.9. From this we see that unlike $t\bar{t}$ and single top-quark, tZ and $t\bar{t}Z$ are much
 266 closer in cross-section and stay closer throughout the range of center of mass energies. This
 267 means that single top-quark analyses must provide stringent $t\bar{t}$ rejection, while the effort
 268 in background removal for tZ will not be as dependant on rejecting $t\bar{t}Z$. The tZ signature
 269 investigated includes three charged leptons, missing transverse energy, and two jets one of
 270 which may be b -tagged [6].

271 Several truth level histograms can be seen in Figures 1.7 and 1.8. Some noteable features
 272 of tZ is the disparity between the eta of the light jet vs. b-quark, the higher p_T of the light
 273 jet compared to the b-quark, the similarity in p_T of leptons from the Z -boson and W -boson,
 274 and the p_T of the neutrino which will manifest as MET.

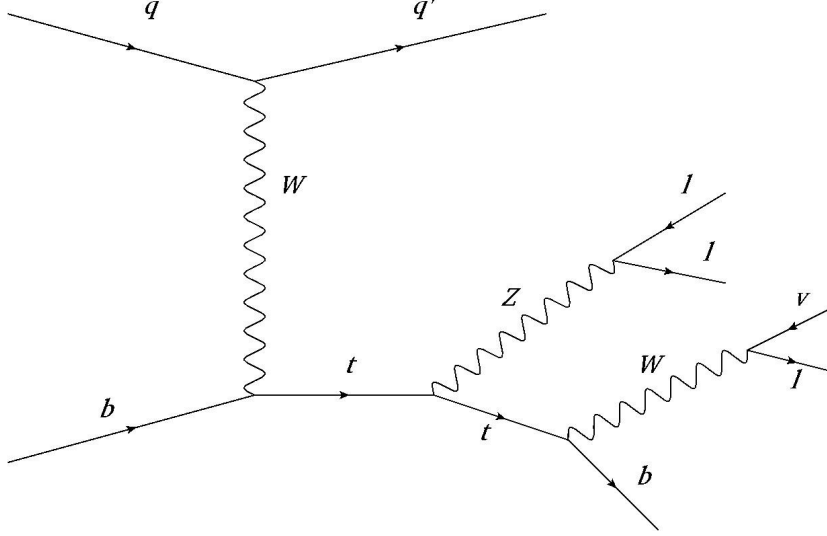


Figure 1.6: Feynman diagram for the tZ associated production going to three leptons [5].

275 tZ can be considered a background to several SM processes. Monotop-quark production
 276 is one of these involving a top-quark and large missing transverse energy. Single top-quark
 277 produced in association with a Higgs boson is a relevant thing to look for to probe the
 278 coupling of a Higgs boson to the top-quark. One can also consider tZ as a background
 279 to Flavor Changing Neutral Current (FCNC) decays from $t\bar{t}$ where one of the top-quarks
 280 decays to a Z boson and a light quark. Aside from being a background to many new physics
 281 searches tZ is also important to measure and has the added bonus of probing the coupling
 282 of the top-quark with a Z boson [6].

283 For this analysis a cut and count method is used. By examining the kinematics of the
 284 particles as we have begun to do in Figures 1.7 and 1.8 regions of phase space can be created
 285 to isolate background regions to ensure proper data modeling through simulation as well as

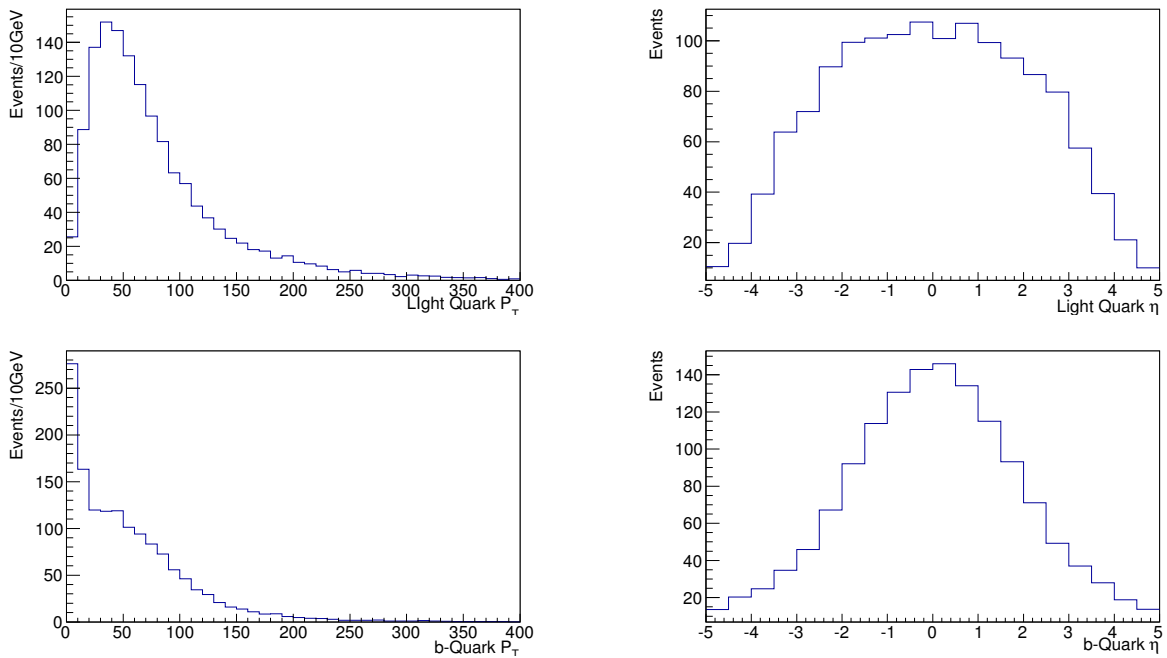


Figure 1.7: Truth information drawn from Madgraph simulation of tZ . Light jet p_T and η as well as b-quark p_T and η .

²⁸⁶ isolating the tZ signal to improve sensitivity for a statistical analysis.

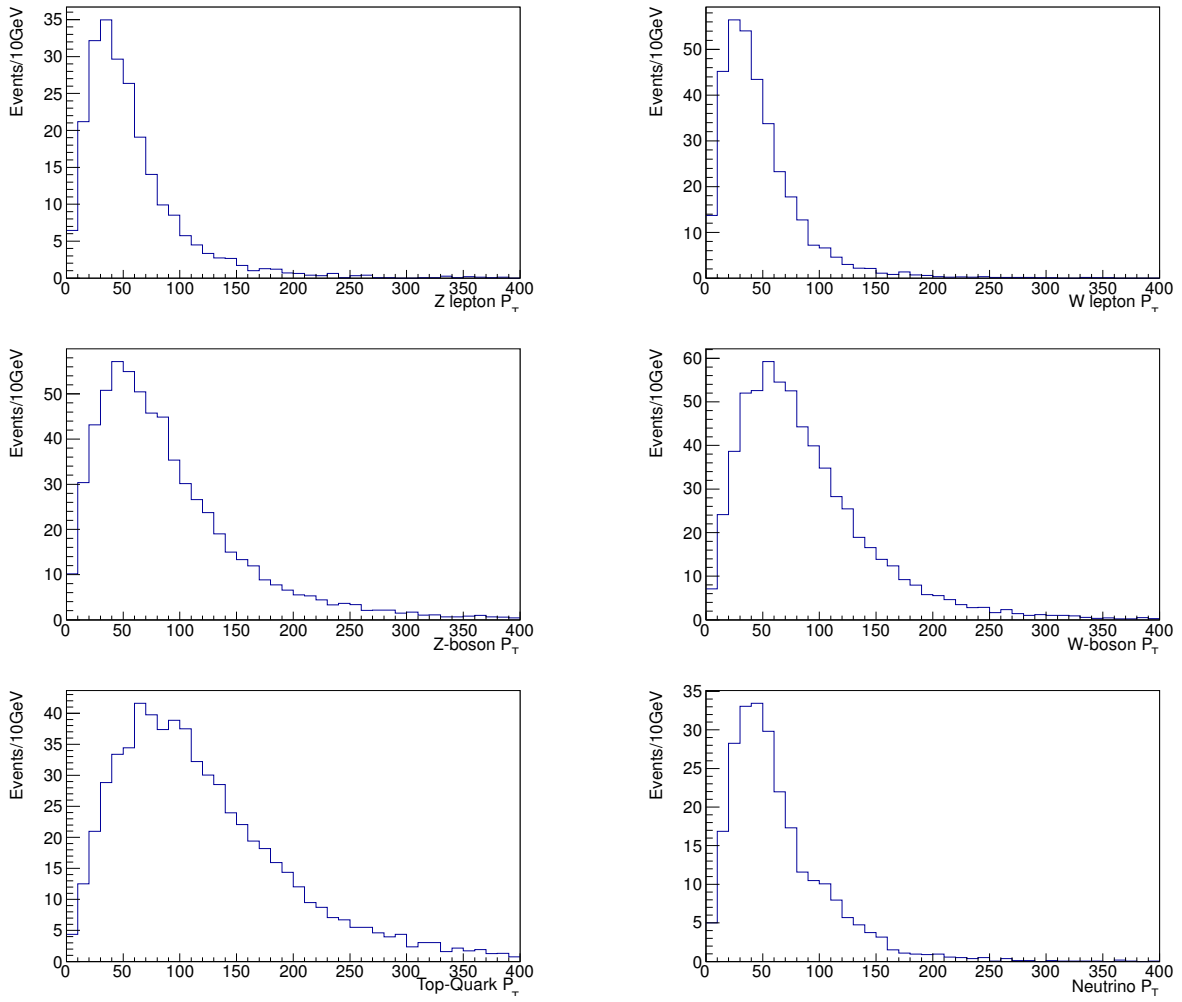


Figure 1.8: Truth information drawn from Madgraph simulation of tZ . The p_T of other objects in tZ .

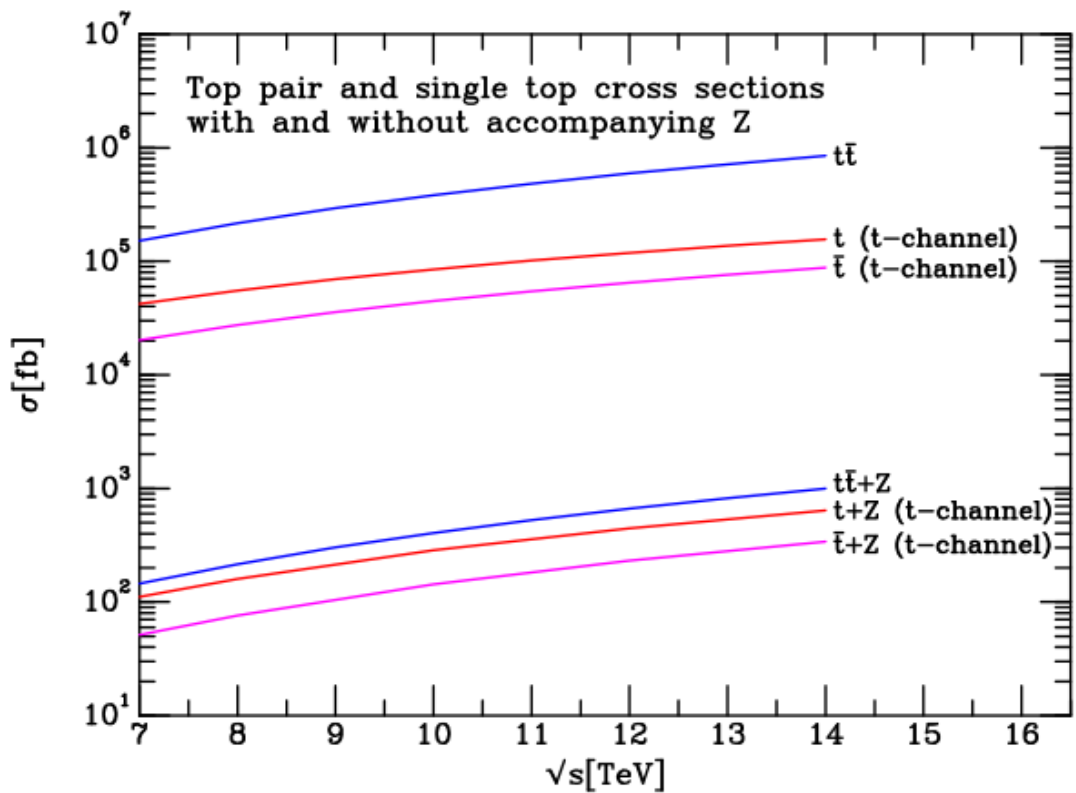


Figure 1.9: Top-Quark pair and single top-quark cross-sections with and without accompanying Z boson [6].

²⁸⁷ **Chapter 2**

²⁸⁸ **CERN, the LHC, and ATLAS**

²⁸⁹ In 1954 the Conseil Europen pour la Recherche Nuclaire(CERN) formed a nuclear physics
²⁹⁰ laboratory just outside of Geneva Switzerland to provide a laboratory needed for physics
²⁹¹ research. CERN has delivered on that promise to give us dozens of experiments that study
²⁹² everything from meteorology to biology. Some of the labs accomplishments include: the
²⁹³ discovery of the W -boson and Z -boson; the determination of the number of light neutrino
²⁹⁴ families; the creation of the world wide web; the creation, isolation, and stabilization of
²⁹⁵ anti-hydrogen for up to 15 minutes; and the discovery of the Higgs boson.

²⁹⁶ Over the past few decades CERN has focused on accelerator physics, housing the Large
²⁹⁷ Electron-Positron Collider (LEP) which ran from 1989 until 2000. LEP was then replaced
²⁹⁸ with the Large Hadron Collider(LHC) starting operations in 2009 after a faulty start in 2008
²⁹⁹ due to a failure in an electrical connection leading to a rupture of the liquid helium enclosure
³⁰⁰ of one of the superconducting magnets. The LHC and LEP are often thought of hand in
³⁰¹ hand because they both used the same 27 km tunnel.

³⁰² **2.1 The Accelerator Chain**

³⁰³ The LHC is capable of colliding protons as well as heavy ions, although we focus primarily
³⁰⁴ on the proton accelerator chain shown in Figure 2.1. The protons used in the LHC start
³⁰⁵ from a hydrogen bottle where a magnetic field strips the electrons from H_2 and the resulting

306 protons are sent through linear accelerator 3(Linac3). Linac3 uses radio-frequency cavities
307 which charge cylindrical conductors which are alternately positively or negatively charged.
308 The conductors directly behind the protons are positively charged while the conductors
309 in front of the protons are negatively charged, with both working to accelerate the protons.
310 Once the protons are through Linac3 they will be bunched with 100ms bunch spacing and will
311 be up to 50MeV in energy [39]. From here it is sent through the 157m circumference Proton
312 Synchrotron Booster(PSB) which accelerate the protons to an energy of 1.4GeV in only 530
313 ms [40]. From there the protons go to the 628m circumference Proton Synchrotron(PS) for
314 tighter bunching of 25ns, and are accelerated to 25GeV [41]. The final step before the LHC is
315 the Super Proton Synchrotron(SPS) which is 7km in circumference. The SPS can accelerate
316 protons to 450GeV in 4.3 seconds [42]. The SPS is notable for the 1983 Nobel prize winning
317 discovery of the W -boson and Z -boson.

318 Finally the protons make it to the LHC to be ramped up to the desired energy for
319 collision. A segment of the LHC beampipe can be seen in Figure 2.2.

320 **2.2 The Large Hadron Collider**

321 It takes approximately 4min 20sec to fill each LHC ring (one in each direction) forming the
322 beams of 2,808 bunches each. After a 20 minute wait time after injection to stabilize and
323 tighten the beams they are accelerated over 25 minutes to an energy of 4TeV per beam.
324 All in all it takes between 5 and 20 seconds to get the protons from Linac2 to the LHC,
325 then 45 minutes to get them up to energy. Once at energy they can be stored for collisions
326 for around 10 hours limited mostly by protons in the beam exchanging momentum between
327 the transverse and longitudinal directions which is enhanced relativistically by a factor of γ .

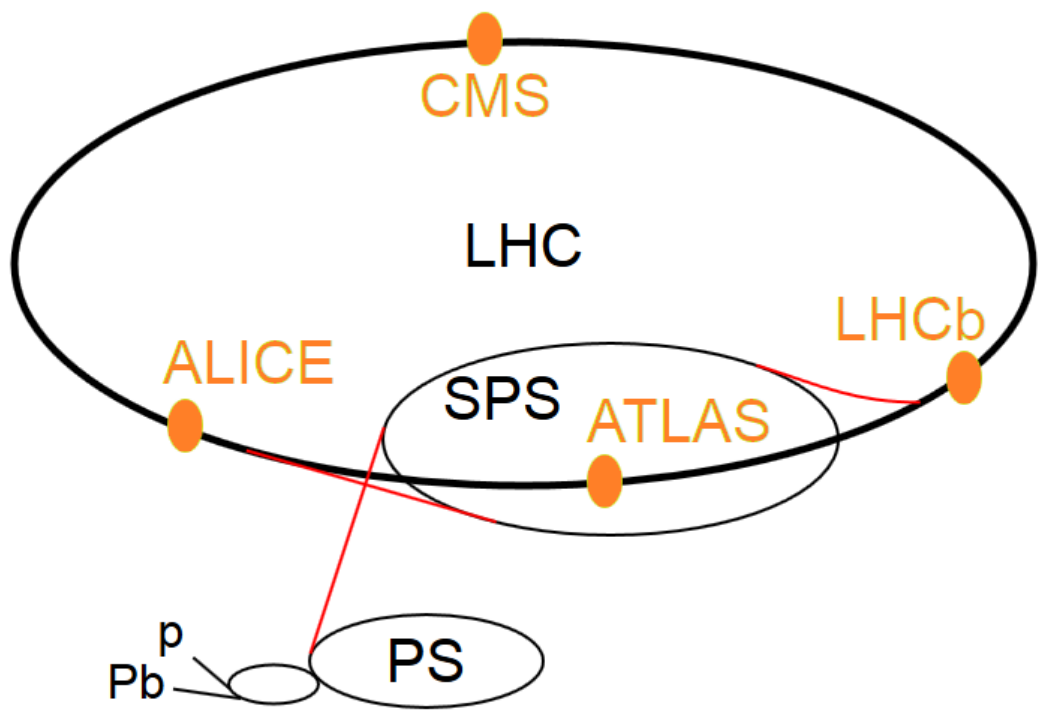


Figure 2.1: Diagram of the accelerator complex for protons to get to the LHC [7].

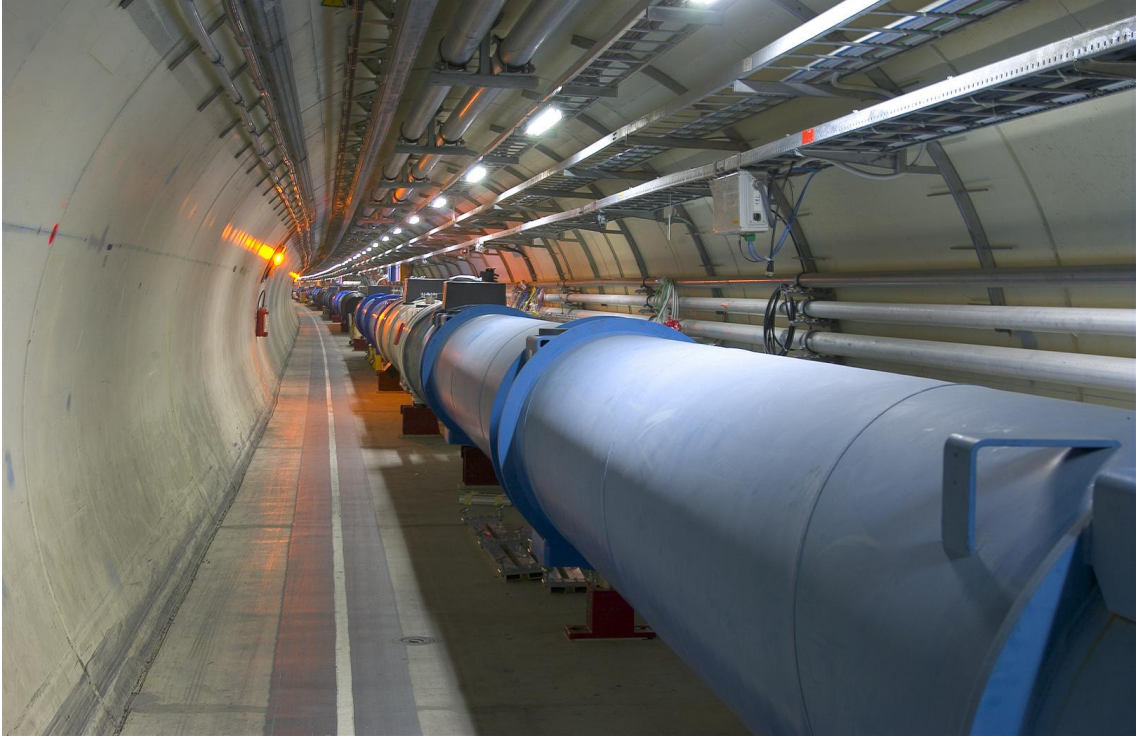


Figure 2.2: A Segment of the LHC beampipe [8].

328 This is known as the Touschek effect. Particles are lost from the beam if their longitudinal
329 momentum deviation is greater than the RF bucket or the momentum aperture of the lattice.
330 After approximately 10 hours of beam collisions the beam is exhausted and is dumped and
331 the injection process is repeated [43] [44].

332 Given the environment necessary for the discovery of new physics the LHC was designed
333 with unprecedented capabilities. While most people think of the LHC as the highest energy
334 collider in the world (which it is) there are more considerations when building an accelerator.
335 In order to discover rare processes we consider instantaneous luminosity in order to collect
336 as many interesting events as can be produced as quickly as possible. Peak ATLAS online
337 luminosity is around $8 * 10^{33} \text{ cm}^{-2} \text{ s}^{-1}$ (as seen in Figure 2.3) which is around 20 times the
338 peak Tevatron luminosity [45] [46]. A greater instantaneous luminosity leads to a greater
339 integrated luminosity, which is a measure of how much data has been collected over time, as

³⁴⁰ seen in Figure 2.4 for previous runs and Figure 2.5 for run 2. The generic term luminosity
³⁴¹ will usually refer to integrated luminosity in this thesis unless otherwise stated.

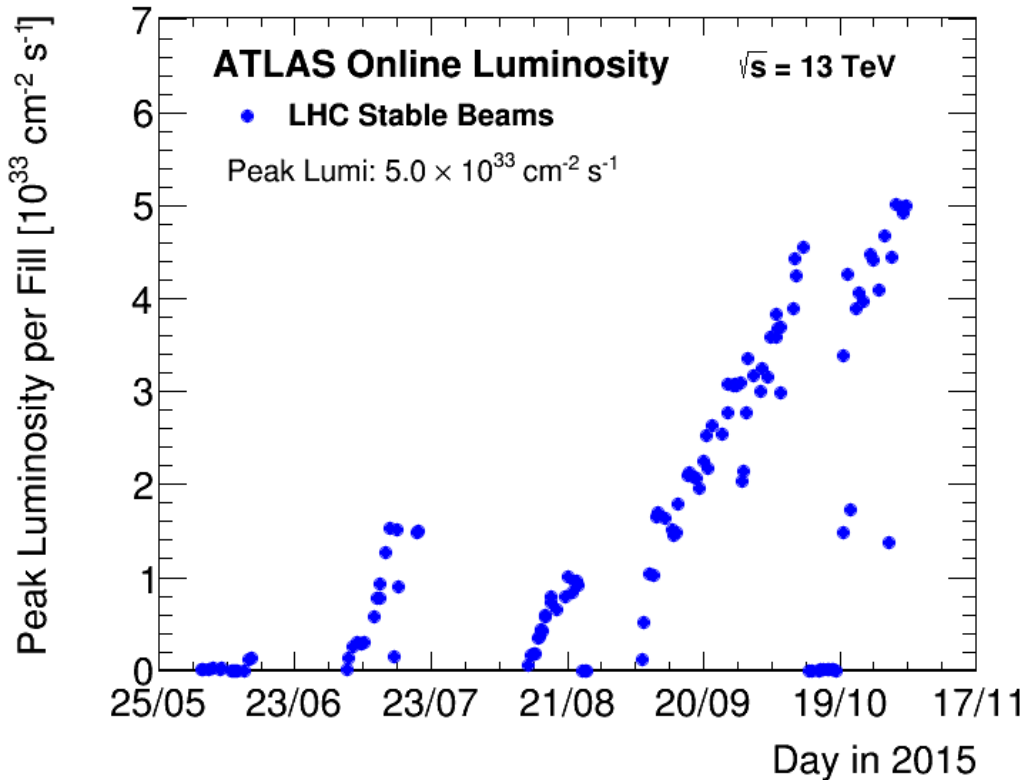


Figure 2.3: Peak instantaneous luminosity over time. As run 2 went on instantaneous luminosity was increased to maximize data collection showing the dramatic increase in data collection in August and September [9].

³⁴²

³⁴³ In order to keep the beams on track and together the LHC has 1232 dipole magnets
³⁴⁴ to steer the beam and 392 quadrupole magnets for focusing and a total of around 9600
³⁴⁵ superconducting magnets. The beams are segmented into 2808 buckets which can be filled
³⁴⁶ with bunches of protons or not. The LHC was designed to deliver bunches that are spaced
³⁴⁷ so that the resulting collisions are 25 ns apart (corresponding to approximately 10 meters
³⁴⁸ between bunches). In practice the LHC operates at 50 ns bunch spacing (leaving every other

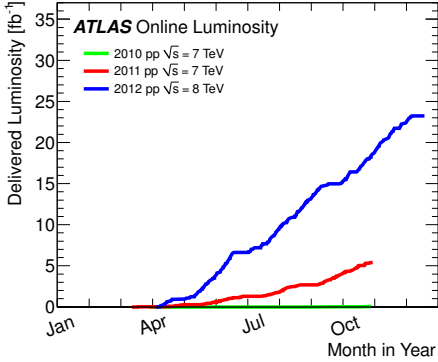


Figure 2.4: Total LHC delivered integrated luminosity over time for run 1 [9]

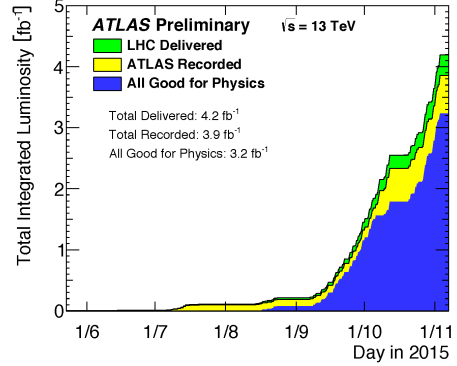


Figure 2.5: Total LHC delivered integrated luminosity over time for run 2 [9]

349 bucket empty) to help with pile up. Pile up is when two separate proton proton collisions
 350 interfere with each other and comes in two forms. Out of time pile up refers to two different
 351 bunch crossings interact with the detector more quickly than the detectors response time.
 352 Running with 50ns bunch spacing helps with out of time pile up while running with 25ns
 353 bunch spacing helps with the other type of pile up, in time pile up. In time pile up is when
 354 two parton collisions happen within the same bunch crossing and both interact with the
 355 detector at the same time. This is designed for and has been increased from the 7 TeV run
 356 with an average of 9.1 interactions per bunch crossing to the 8 TeV run with 20.7 interactions
 357 per bunch crossing as seen in Figure 2.6 with a more conservative 13.7 interactions per bunch
 358 crossing for run 2 as seen in Figure 2.7. Pile up is an important consideration in triggering
 359 and is discussed in this capacity in chapter 3 [43] [44].

360

361 With an accelerator of this magnitude and a diversity of possible research topics, investi-
 362 gation through multiple experiments is merited. CMS and ATLAS are the largest general
 363 purpose detectors designed to search for the broadest range of possible new physics mod-

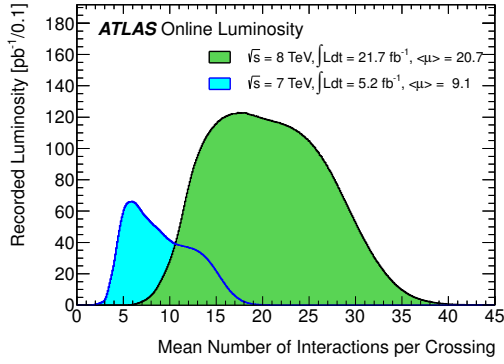


Figure 2.6: Number of interactions per crossing is a measure of in time pile up. This is comparing the number of interactions per crossing in the LHC 7 TeV run and the 8 TeV run [9].

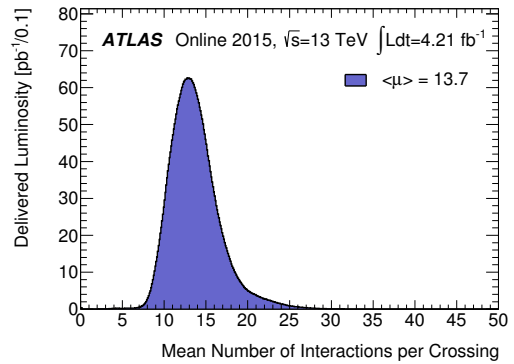


Figure 2.7: Number of interactions per crossing is a measure of in time pile up. This figure is for run 2 which is in comparison to Figure 2.6 which is for run 1 [9].

364 els and precision measurements. MoEDAL searches for magnetic monopoles. TOTEM and
 365 LHCf are looking for forward particles and are positioned near CMS and ATLAS respectively.
 366 ALICE was specially designed to study heavy ion collisions at the LHC to search for
 367 a state of matter known as quark gluon plasma. LHCb is an asymmetric detector studying
 368 the effects of matter antimatter asymmetry in proton proton collisions.

369 With the LHC at such high energies and luminosities detectors had to be designed like
 370 never before to be fast, radiation hard, and finely segmented all while maintaining a sensible
 371 budget.

372 2.3 ATLAS

373 A Large Toroidal LHC AparatuS (also known as ATLAS or the ATLAS detector) is among
 374 the largest and most complex particle detectors in the world and can be seen schematically
 375 in Figure 2.10 but a more impressive view in Figure 2.8 shows its namesake toroidal magnets
 376 in full view before much of the detector was added. It utilizes a multilayer design which has

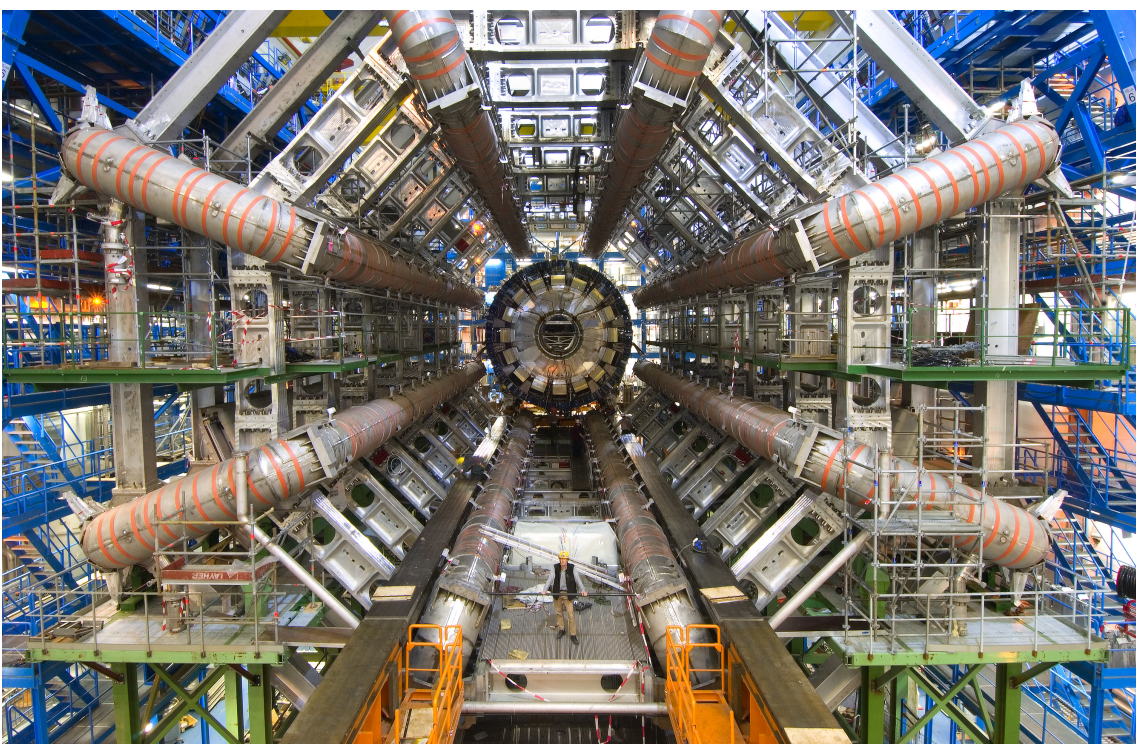


Figure 2.8: ATLAS with its namesake toroidal magnets prominently visible [10].

377 become ubiquitous in high energy physics. With this multilayer design comes a coordinate
 378 system that is vital to the design and use of the detector. There is a Cartesian coordinate
 379 system superimposed in ATLAS with the \hat{y} coordinate running vertically to the surface, the
 380 \hat{x} coordinate running toward the center of the LHC ring, and the \hat{z} coordinate running the
 381 length of ATLAS pointing in the counter clockwise direction around the LHC ring when
 382 viewed from above. With this there is also a spherical coordinate system defined with ϕ
 383 running around the detector sweeping from the \hat{x} axis toward the \hat{y} axis while θ runs away
 384 from the \hat{z} axis. While useful for construction and planning purposes, these variables are not
 385 as useful for analysis. For analysis a Lorentz invariant variable is desirable so a particles
 386 properties in the detector can be measured in any reference frame. One is rapidity, defined
 387 as

$$y = \frac{1}{2} \ln \left(\frac{E + p_z}{E - p_z} \right) \quad (2.1)$$

388 which has the unfortunate property of being dependent on the particle mass. Another is the
 389 widely used pseudorapidity, defined as

$$\eta = \frac{1}{2} \ln \left(\frac{|\vec{p}| + p_z}{|\vec{p}| - p_z} \right) \quad (2.2)$$

390 which can be rewritten in terms of detector geometry variables as

$$\eta = -\ln \left(\tan \left(\frac{\theta}{2} \right) \right) \quad (2.3)$$

391 where $\eta = \infty$ corresponds to the beamline. η is Lorentz invariant as long as $m \ll E$ which is
 392 in the low mass regime. In this regime pseudorapidity approximates rapidity. Pseudorapidity,

393 therefore, has both the properties of describing detector geometry and describing particles
394 in the detector that have boosts along the \hat{z} axis [13].

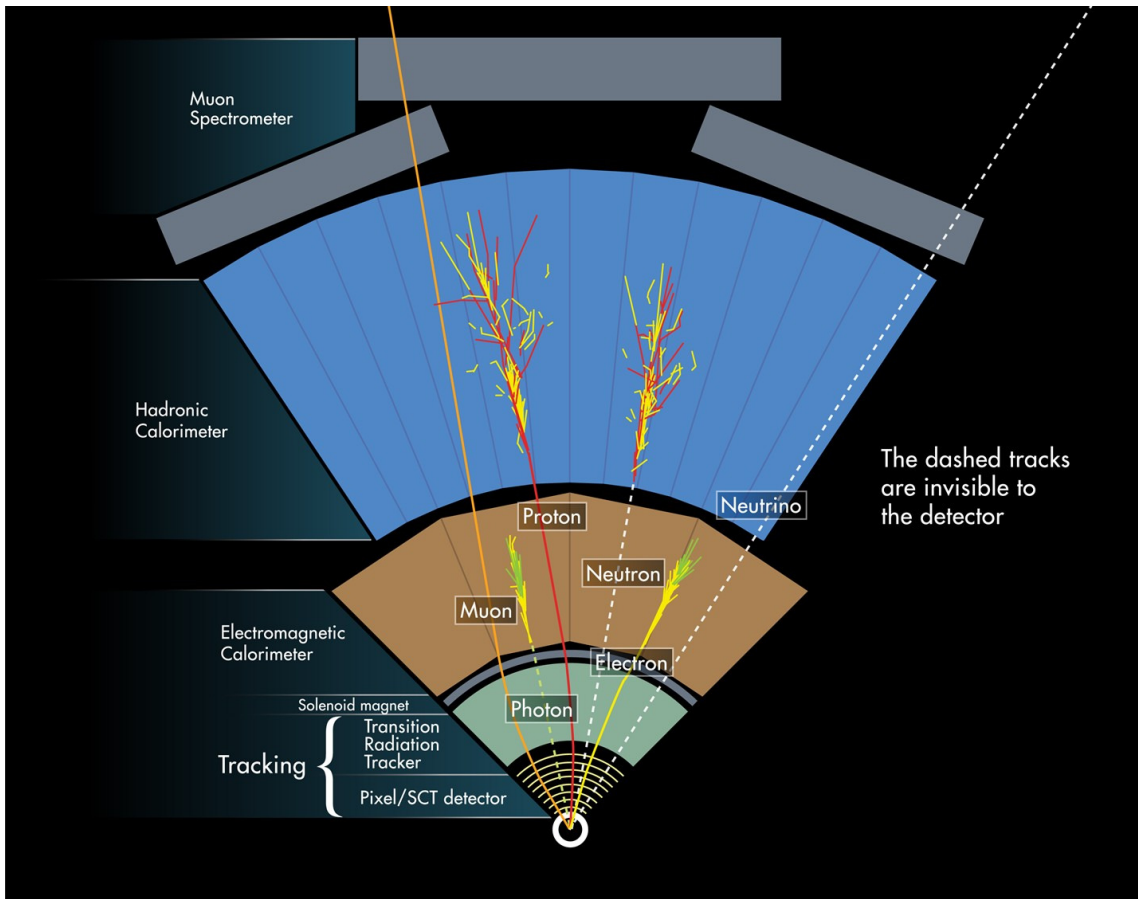


Figure 2.9: A figure diagramming how particle identification can be achieved using multiple layers of the detector [11].

395 ATLAS can be segmented into several parts. The inner detector, the calorimeters, the
396 muon spectrometer, and the magnets. Overall these systems are designed to work together
397 to give measurements of particle energies as well as particle identification as diagrammed in
398 Figure 2.9. An electron can be identified by tracks in the inner detector and a shower in the
399 electromagnetic calorimeter, distinguished from the photon by the tracks in the inner detec-
400 tor. Meanwhile jets get stopped in the hadronic instead of the electromagnetic calorimeter
401 and muons will go all the way through the detector leaving tracks all the way. Many particles

402 like the Z -boson and top-quark decay before reaching the detector. These objects must be
403 reconstructed from their decay products. Neutrinos can be difficult to reconstruct because
404 they go through the entire detector without interacting at all. More on object reconstruc-
405 tion is described in chapter 5 but for now we can take a deeper look into the subsystems of
406 ATLAS .

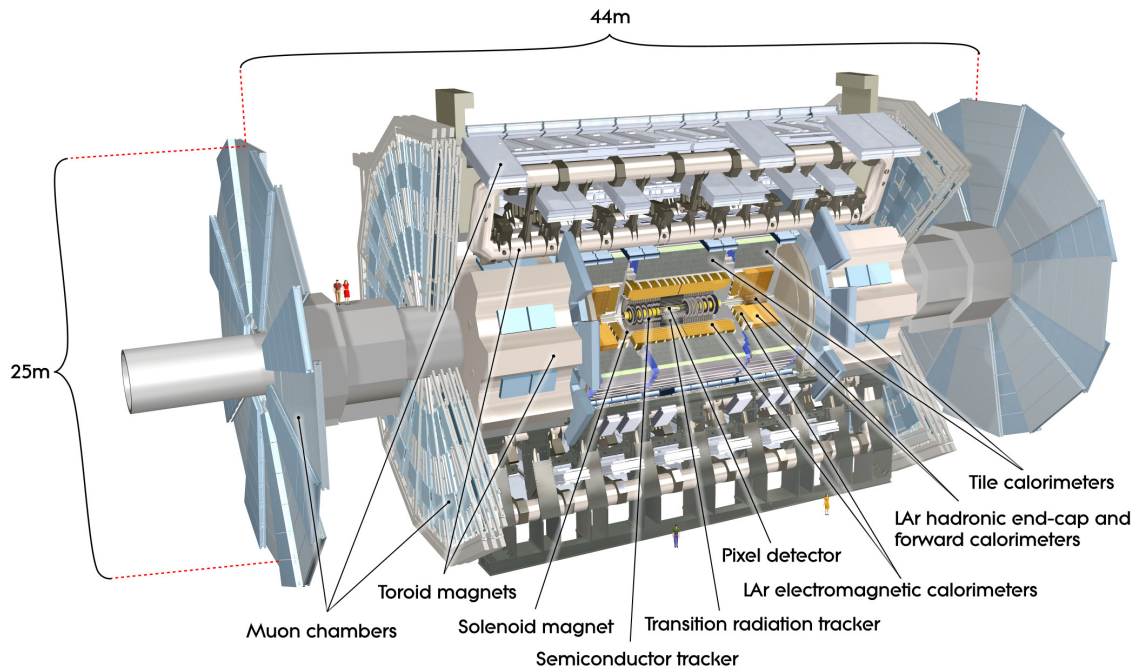


Figure 2.10: Cutaway diagram of ATLAS [12].

407 2.3.1 Magnet System

408 ATLAS has a magnet system designed to assist in particle identification by curving the
409 path of charged particles through the detector systems. There are three parts to the magnet
410 systems; the solenoidal magnet around the inner detector, the barrel toroids, and the endcap
411 toroids. A schematic diagram of the layouts of these magnets can be seen in Figure 2.11.
412 The magnetic field can be seen in Figure 2.12.

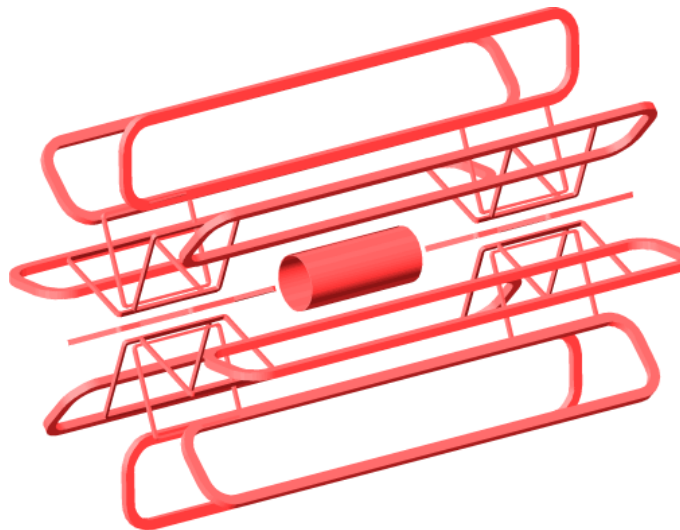


Figure 2.11: Illustration of the ATLAS magnet system, showing the barrel solenoid, barrel toroid, and endcap toroid coils [13].

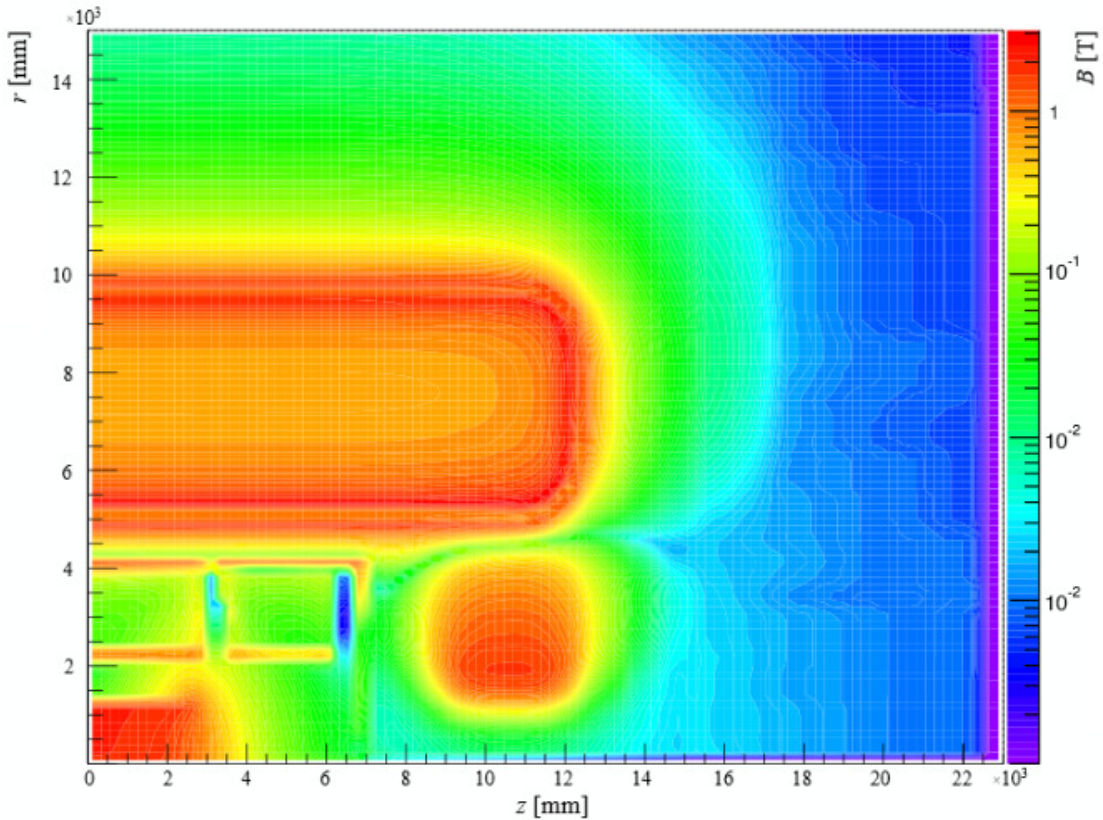


Figure 2.12: A mapping of the magnetic fields in atlas. Note the inhomogeneous nature of the toroidal field and the comparative constant nature of the solenoidal field [14].

413 The solenoidal magnet provides a nearly uniform 2T magnetic field for the inner detector.
414 The Solenoid is designed to be as thin as possible to minimize the interaction of the particles
415 from physics events to aid in calorimetry. Any interaction in the solenoid will begin the
416 showering process which means energy from the interacting particle will be lost and will
417 have to be accounted for in calorimetry.

418 The eight barrel toroids are visible in Figure 2.8 and run $\eta < 1.6$ providing a peak
419 magnetic field of 3.9T around the muon spectrometers and are highly irregular as seen in
420 Figure 2.12. Because of this irregularity the magnetic field must be mapped carefully for
421 accurate muon tracking.

422 The endcap toroids complete the ATLAS magnet systems providing a peak magnetic
423 field of 4.1T for the forward detectors at $1.4 < \eta < 2.7$. The endcap magnets are offset from
424 the barrel toroids by $\frac{1}{16}$ of a turn so that they bisect the angle (in ϕ) between the barrel
425 toroids seen in Figure 2.12.

426 These magnets are crucial for particle identification and momentum measurements of
427 charged particles and are strategically placed around the detector subsystems described
428 hereafter. [47]

429 2.3.2 Inner Detector

430 The inner detector provides tracking information for tracked particles close to the beamline.
431 Track reconstruction is finding sets of measurements coming from one charged particle and
432 building the associated trajectory through the detector. In order to achieve this the inner
433 detector was designed to be as hermetic as possible with high granularity as close to the
434 beamline as possible.

435 The inner detector has three parts and can be seen in its entirety in Figure 2.14. Those

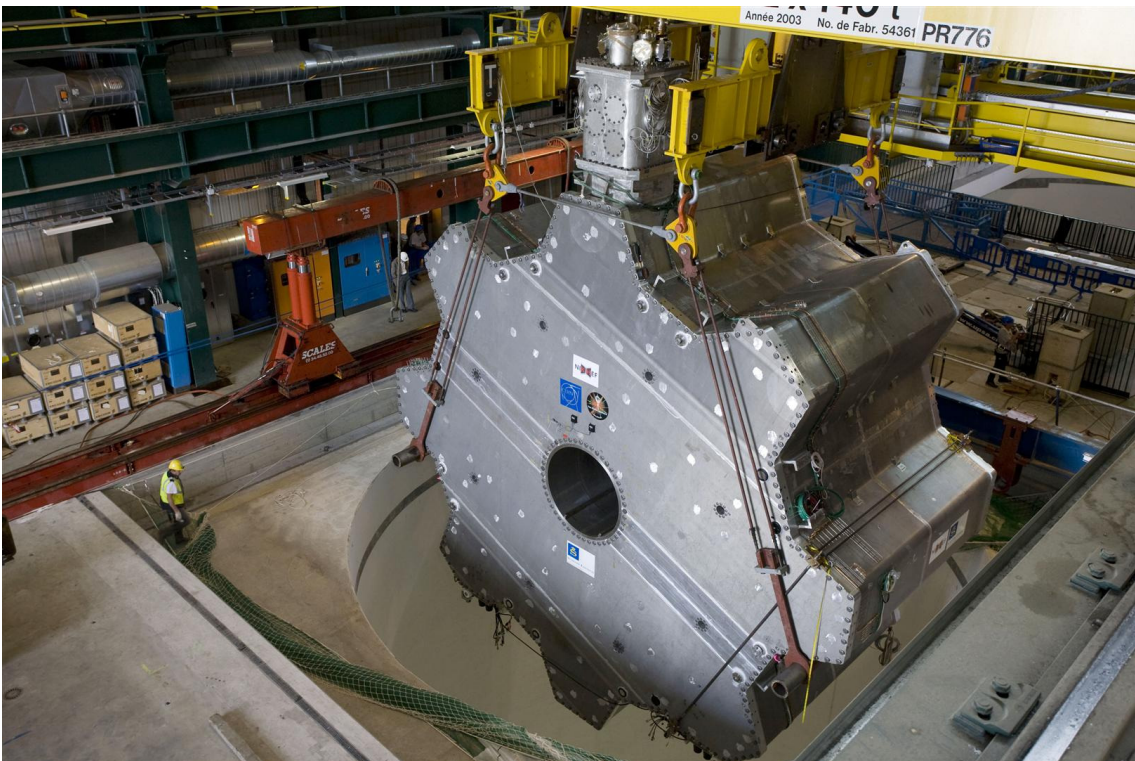


Figure 2.13: Preparation for lowering an endcap magnet into the ATLAS cavern [15].

⁴³⁶ parts are the pixel detector, the SemiConducting Tracker (SCT), and the Transition Radia-
⁴³⁷ tion Tracker (TRT) [48].

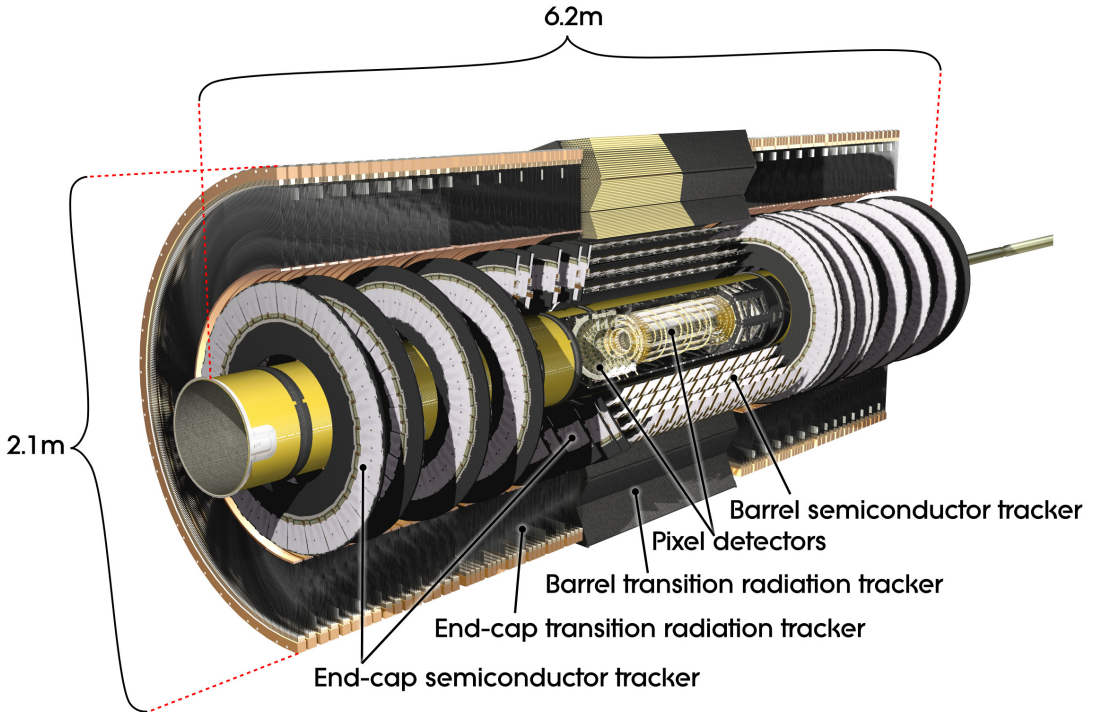


Figure 2.14: Cutaway diagram of the ATLAS inner detector [16].

⁴³⁸ The pixel detector and the SCT work on ionization of silicon which is separated into
⁴³⁹ positive and negative charges which can be separated by an electric field into read out
⁴⁴⁰ electronics. The read out can be either binary or non-binary. A binary read out registers
⁴⁴¹ a hit over some threshold or doesn't. The non-binary readout registers the charge collected
⁴⁴² over time over some threshold and reports the amount of charge collected to assist in track
⁴⁴³ reconstruction. Non-binary readouts give better tracks, but are more expensive and the read
⁴⁴⁴ out electronics take up more space in the valuable real estate near the beamline. The pixel
⁴⁴⁵ detector and SCT cover $\eta < 2.5$. [49] [50]

⁴⁴⁶ The SCT strip detectors use a stereo-angle technique to get position measurements where

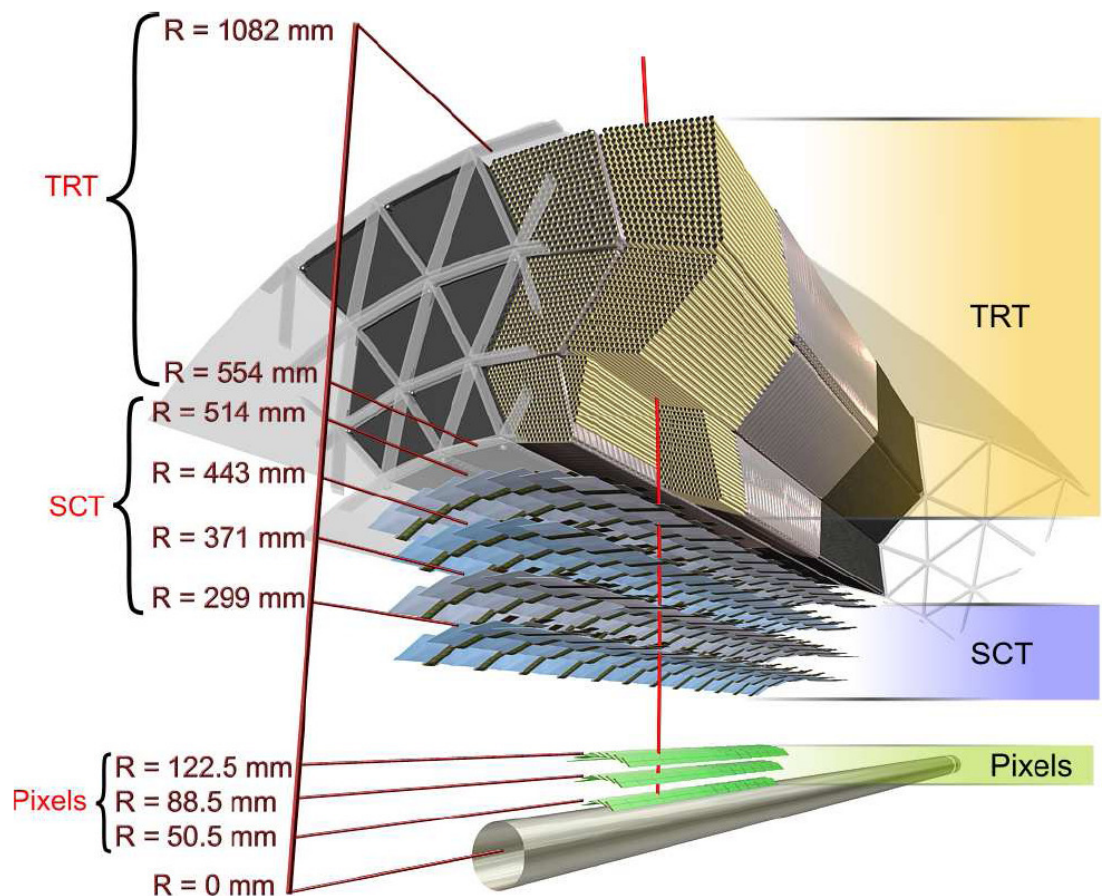


Figure 2.15: A diagram of the sub detectors of the inner detector with relative radial positions [13]

447 concentric layers are constructed so a small angle (40 mRad) gives position measurement.
448 Without an angle between layers of the strip detector only a ϕ could be read out, but with
449 the angle a η can be read out as well. By using strips of silicon a lot of money and space
450 can be saved in comparison to pixel detectors mostly in read out electronics and there wont
451 be as much supporting material in the way for the calorimeters. [51] [52] [53]

452 The TRT works on the principle of transition radiation. When a high energy particle goes
453 between media with differing dielectric constants, the result will be the emission of radiation
454 or as Jackson puts it “the fields must reorganize themselves as the particle approaches and
455 passes through the interface. In this process, some pieces of the fields are shaken off as
456 transition radiation”. [54] The TRT uses this by filling tubes with a gas of Xe , CO_2 , and O_2
457 which is ionized by charged particles passing through. All charged particles will interact with
458 the TRT giving tracking information, but the TRT has two separate thresholds for readout.
459 The first threshold tracks charged particles while the second higher threshold determines
460 if transition radiation is being detected. Because the electron participates in transition
461 radiation more strongly than the pion we can obtain good pion rejection while maintaining
462 electron reconstruction efficiency. [55] [56] [57]

463 The largest source of track reconstruction inefficiency is hadronic interaction. When a
464 hadron interacts with the nucleus of the detector material it is usually destroyed, and creates
465 a hadronic and electromagnetic shower. When this happens the primary track stops and a
466 series of other tracks begin, but unfortunately the track can not be reconstructed. Another
467 problem is electron bremsstrahlung. When a charged particle passes near the nucleus of
468 the detector material it will radiate, loosing energy. This effects electrons more than other
469 particles because the energy loss as it traverses the detector is proportional to energy over
470 mass squared ($\frac{dE}{dx} \propto \frac{E}{m^2}$) so the light electron will brem more strongly than its heavier coun-

⁴⁷¹ terparts. Another consideration in tracking is multiple scattering which can cause a random
⁴⁷² change in direction not caused by curvature in the magnetic field. The method of detection
⁴⁷³ can actually be a problem as well because when the particle ionizes the atoms of the detector
⁴⁷⁴ it loses energy [14].

⁴⁷⁵ 2.3.3 Calorimeters

⁴⁷⁶ There are two calorimeter systems for detecting electromagnetically interacting particles and
⁴⁷⁷ strongly interacting particles referred to as the electromagnetic calorimeter and hadronic
⁴⁷⁸ calorimeter respectively as seen in Figure 2.16. One high energy particle from the hard
⁴⁷⁹ interaction of an event will shower into many particles creating a wave of energy deposition
⁴⁸⁰ in the calorimeters. This process is particularly useful for neutral particles that can not be
⁴⁸¹ tracked in the inner detector, but is also useful for a more complete picture of a particular
⁴⁸² object.

⁴⁸³ Both the electromagnetic and hadronic calorimeters work on several different types of
⁴⁸⁴ interactions. The first is radiative interactions where the incoming particle will scatter off a
⁴⁸⁵ constituent atom creating a Rutherford scattering type interaction. When they aren't hard
⁴⁸⁶ scattering off a nucleus they can also Compton scatter off atomic electrons, ionize the atoms
⁴⁸⁷ of the detector, or have other similar low momentum transfer interactions. After this particle
⁴⁸⁸ energies fall to when they are absorbed by atomic interactions and the number of particles
⁴⁸⁹ in the shower begins to fall. It is often noted that muons and protons are minimally ionizing
⁴⁹⁰ in the electromagnetic calorimeters. This is because the radiative interactions which begin
⁴⁹¹ the particle cascade fall by m^2 , so their large mass gets them through the electromagnetic
⁴⁹² calorimeter [58].

⁴⁹³ In ATLAS our Liquid Argon (LAr) calorimeters use sampling calorimetry. Because the

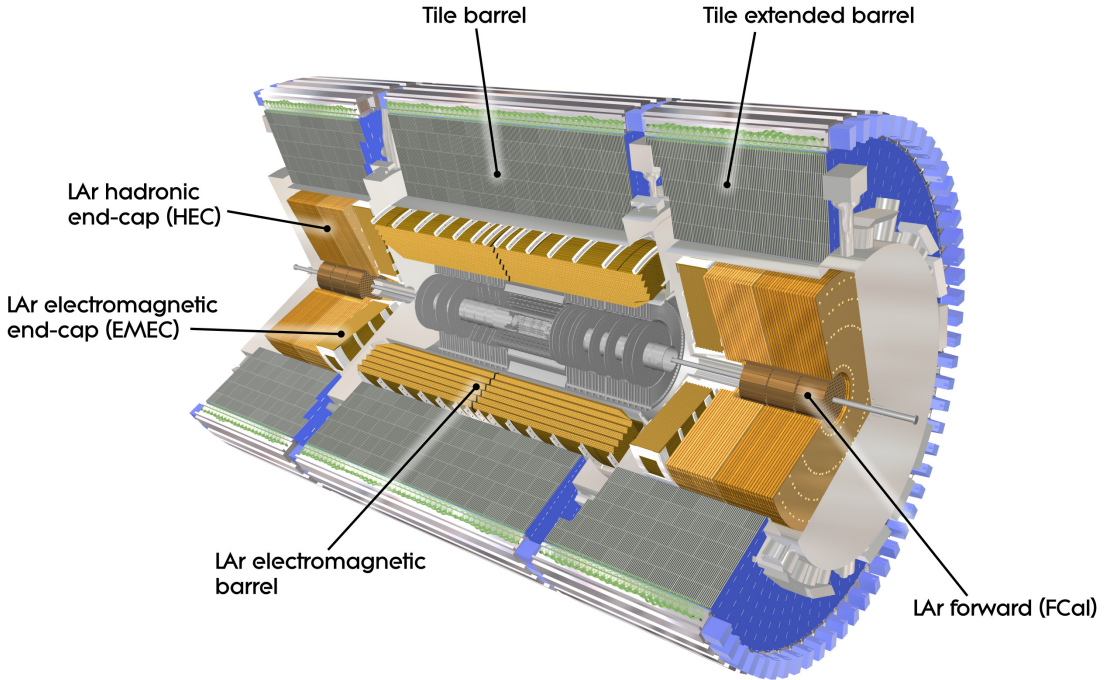


Figure 2.16: Cutaway diagram of the ATLAS calorimeter systems [17].

494 primary interactions are radiative in nature it is desirable to have high atomic number in the
 495 calorimeter material. The principal of sampling calorimetry is to have two materials in the
 496 calorimeter; one to facilitate the radiative interaction and begin the showering process, and
 497 another to accommodate the lower energy interactions that provide the signal that is read
 498 out. In ATLAS the LAr calorimeter is accordion shaped lead coated with stainless steel
 499 for radiative interactions with liquid argon to collect the resulting shower. The accordion
 500 shape is useful to increase the path length of particles in the material, thereby increasing
 501 the probability of an interaction and lowering the total amount of material needed. In the
 502 liquid argon are wires held at high voltage to attract the ionized particles and read out the
 503 charge current generated [58].

504 In ATLAS we also have tile calorimeters(TileCal). They work on the same principles as

505 the LAr calorimeters. The sampler for the TileCal is sheet steel without the accordion shape,
506 and the readout material is a collection of plastic scintillators that emit light when hit with
507 the resulting shower. The plastic scintillators are coupled to optical wavelength shifting
508 fibers to redirect light to photomultiplier tubes. The light emitted from the scintillating
509 plastic is typically in the UV range, and is shifted into the blue or green visible wavelengths
510 to help limit attenuation while propagating [59] [60].

511 The geometry of the calorimeter systems are complex, but a simplified version is given
512 here and can be seen in Figure 2.16. The barrel region of the detector (with $\eta < 1.475$)
513 has both LAr calorimetry and TileCal [61]. The endcap calorimeters cover $1.375 < \eta < 3.2$
514 [62]. There is also a LAr forward calorimeter(FCal) that covers the extremely forward region
515 $3.1 < \eta < 4.9$ with a copper absorber for the electromagnetic portion and a tungsten absorber
516 for the hadronic part. There is also an inner presampler to catch how intensively radiative
517 interactions from interactions with the inner detector took place [63].

518 2.3.4 Muon Systems

519 Muons provide an interesting challenge because they do not interact strongly with the elec-
520 tromagnetic or hadronic calorimeters and pass through the detector. The muon systems have
521 four layers shown in Figure 2.17; they are the Monitored Drift Tubes (MDT), the Cathode
522 Strip Chambers (CSC), the Resistive Plate Chambers (RPC) and the Thin Gap Chambers
523 (TGC).

524 The MDT provides most of the precision muon tracking in ATLAS. The MDT has a barrel
525 and endcap section. The barrel section covers $\eta < 1.0$ while the endcaps cover $1.0 < \eta < 2.7$.
526 The MDT works on ionizing gases and is composed of straw tubes filled with gas which is
527 composed of argon, nitrogen, and methane. The muon traverses the straw tube and ionizes

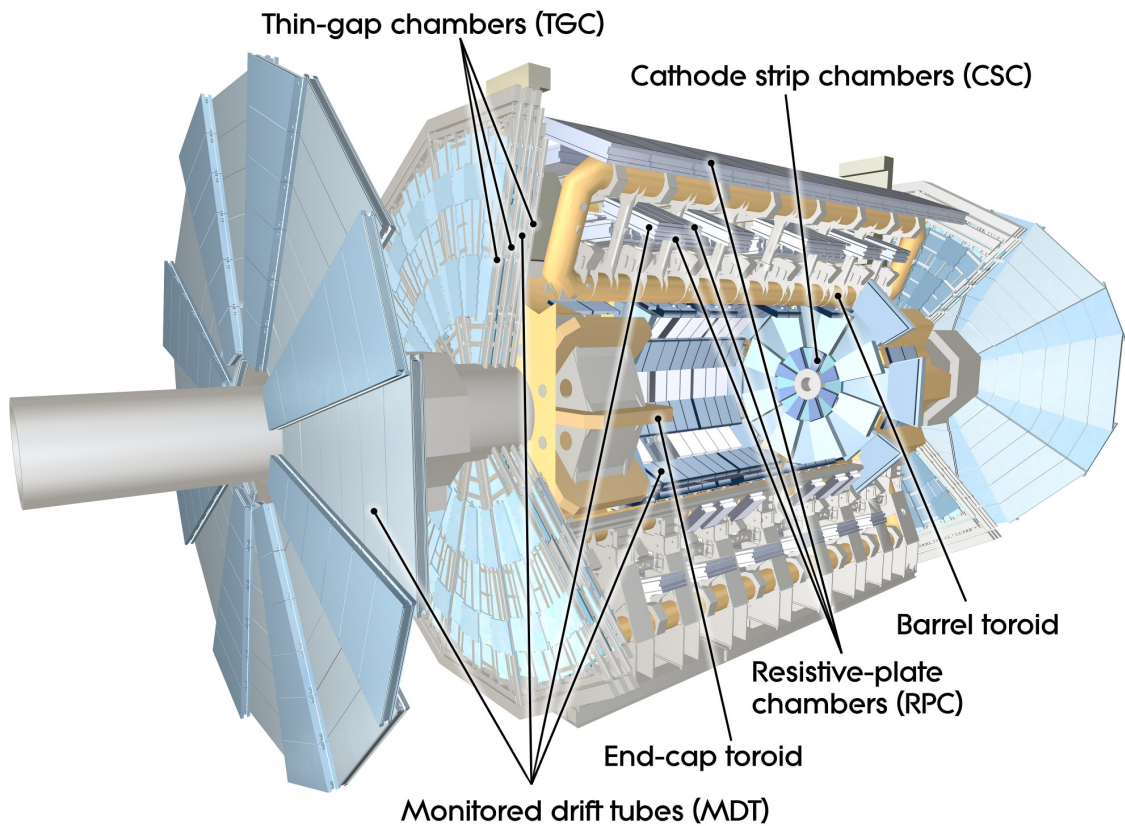


Figure 2.17: Cutaway diagram of the ATLAS muon spectrometer and toroid magnet systems [18].

528 the gas and the resulting charged particles are collected on a wire in the center of the tube
529 which is held at high voltage. The amount of time it takes from the first current to reach
530 the center wire until the last current reaches the center wire tells us how far away the muon
531 came to the center of the tube. With this information we can make measurements on the
532 path of the muon.

533 The CSC are multiwire proportional chambers used in high radiation zones around AT-
534 LAS at $2.0 < \eta < 2.7$. They work on the same principles as the MDT, but with a different
535 gas mixture.

536 The RPC is designed to supplement the MDT in the barrel region $\eta < 1.05$ and has a
537 fairly simple design. Each RPC chamber is two resistive plates held at 8900V across a 2mm
538 gap. An incoming charged particle will ionize the gas and cause a localized discharge of the
539 capacitor. The location of this discharge can then be read out. This method does not give
540 very good spacial resolution (approximately 1 cm) but is quite fast with a timing uncertainty
541 of 1.5 ns. Because of this it is utilized primarily by the Level 1 trigger.

542 The TGC (as seen in Figure 2.18) is also designed to supplement the MDT but in the
543 forward region of the detector $1.05 < \eta < 2.4$. It uses the same technology as the RPC
544 and consequently is used for triggering as well. The TGC has a different gas mixture in
545 order to decrease spacial resolution for bunch identification (down to 9 mm) but suffers
546 in timing response (7ns) which is still fast enough to be used by the level 1 trigger sys-
547 tem. [64] [65] [66] [67]

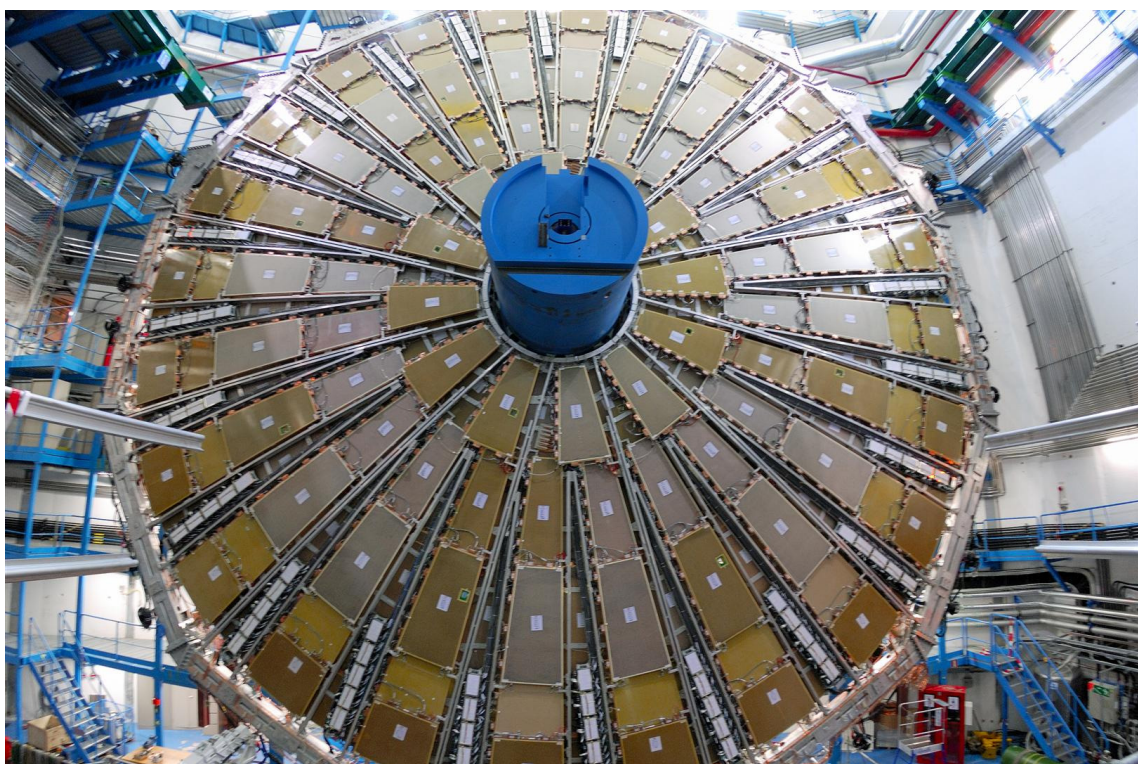


Figure 2.18: The TGC wheel [19].

548 **Chapter 3**

549 **The Trigger System on ATLAS**

550 Interaction rates in the ATLAS detector are staggering. Since we can not store information
551 on every interaction we must filter it through the ATLAS trigger system and keep only
552 events which have the prospects to contain interesting processes. There are three terms
553 worth defining here. The trigger is the decision making process used by ATLAS to dis-
554tinguish interesting events from non-interesting ones, Data acquisition refers to the system
555 that delivers and stores wanted events and variables, and data preparation which prepares
556 saved data for analysis. The trigger is separated into three levels that start with hardware
557 on the detector and get more computationally intensive as they progress. They are Level1,
558 Level2, and Event Filter. A trigger chain is a set of trigger settings that can be designed
559 around hardware responses, reconstructed objects, and reconstructed events. There are ap-
560proximately 700 different trigger chains. With so many types of events to be seen we must
561 limit the rate of any given trigger chain due to bandwidth considerations. With this in mind
562 every proposed trigger chain is evaluated for efficiency, purity, overall rate, overlap rate with
563 other trigger chains, response to pile up, response to increased luminosity, and its usability
564 in many analysis or at least one well motivated analysis.

565 This system was designed with four main principles in mind.

- 566 1. Factorization and partitioning
- 567 2. Minimization of data movement

568 3. Uniformity and minimization of required developments

569 4. Staging of data volumes and rates

570 Partitioning of the trigger into relevant components is important so that various subsys-
571 tems can run independently and concurrently. The capacity to run with only a fraction of
572 the trigger chains was deemed important to be able to debug existing trigger chains as well
573 as be able to commission new trigger chains. Minimizing data movement is key to keeping
574 high rates of throughput with low latency. Uniformity allows adoption of common hardware
575 that can be purchased more cheaply and replaced more easily. Staging the trigger into three
576 levels was done in part to keep the trigger adaptable so as the physics environment changed
577 the trigger could be adapted or expanded.

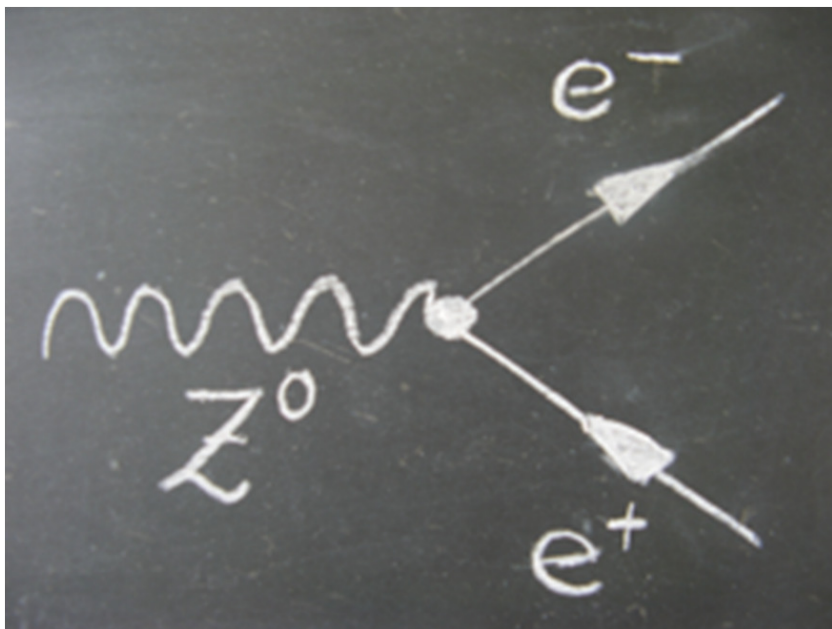


Figure 3.1: A Z -boson decaying to an electron positron pair.

578 If problems arise with a trigger chain they can be dealt with in several ways. The first tool
579 of evaluation of many triggers is the tag and probe method. In this method two objects can
580 be selected from an event, one of which (known as the tag) will be given a tight requirement

581 to ensure purity of a particular sample while the other (known as the probe) is taken to
582 be tested on. An example is a Z -boson going to two electrons with one electron being a
583 tag while the other is a probe to test the efficiency of the single electron trigger chain. The
584 Feynman diagram can be seen in Figure 3.1. The probe is then classified into three groups;
585 passing the tag criteria, passing the probe criteria, or failing the probe criteria. Once we
586 know how the electron failed we can take steps to correct the inefficiency. If the trigger
587 rate is too high we will not be able to record events that pass the trigger. In this case it is
588 common to use prescales. Prescales reject a given percentage of events that would otherwise
589 pass a trigger chain in order to make bandwidth for other trigger chains. Their use is often
590 motivated by the generality or usefulness of the trigger chain and political will to keep events
591 from that trigger chain.

592 **3.1 Level 1 Trigger**

593 The Level1(L1) trigger is hardware based and looks at each segment of each subdetector
594 individually to determine if the event should be passed. The L1 trigger is composed of
595 several parts. L1Calo looks at the level of calorimeter deposits and their multiplicity while
596 L1Muon looks at the muon systems in the same way. the L1 trigger also has front end analog-
597 digital processing (the hookup to the actual detector), the L1 buffer to store information for
598 long enough to accommodate L1 latency, the derandomizing buffer where L1Accept signals
599 are stored to be sent to the L2 trigger, buses for transmitting the front end data stream
600 to the back end electronics, the Central Trigger Processor(CTP) which is the brains of the
601 trigger system and makes the decisions on each event based on a premade trigger menu, the
602 Trigger Timing Control(TTC) which is responsible for ensuring that all individual detector

603 readouts are synchronized and properly labeled by bunch crossing and interaction point, and
604 the Region of Interest Builder(RoIB) which prepares passed events for L2.

605 There are four main environmental considerations that influence the design of the front
606 end readout electronics; radiation effects, magnetic fields, space around the detector for
607 access, and the location of the service caverns housing the back end electronics. Radiation
608 is a concern because, for example, read out electronics can be falsely triggered by radiation
609 energy. Magnetic fields dictate the composition of components in the electronics especially
610 in power supplies. Access is problematic in areas where there is a lot of detector material
611 with little room for read out electronics such as the inner detector. The service caverns can
612 house electronics without worries about radiation, and thus can house electronics that would
613 otherwise be unavailable in the cavern. The types of links are then defined by the type of
614 data being transmitted (analog or digital) as well as the speed it is transmitted through the
615 length of the links which ranges from 50 to 150 meters. [64] [67]

616 The L1 trigger takes the potential data rate from 20 MHz to 75 kHz in a latency of less
617 than $2.5 \mu\text{s}$ including propagation delays the cables to get the information to the trigger logic
618 circuit [64]. Latency is the time delay from detector response to the actual trigger decision.
619 Because of the need for such low latency L1 considers information on calorimetry and muon
620 systems but not information on tracking because the reconstruction algorithms required are
621 too slow. [67]

622 **3.2 High Level Trigger**

623 The HLT is the name given to the portion of the trigger that is largely software based. It is
624 designed to run on common computer hardware and computing cores from L2 and EF are

625 often interchangeable (and in fact they are interchanged regularly).

626 The Level2(L2) trigger is software based and looks at Regions of Interest(RoI) passed to
627 it by L1. The use of these RoIs in software make the L2 trigger common hardware, allowing
628 for 500 identical PCs to be used. These RoIs give more information to make decisions and
629 are given more time to make those decisions in. The L2 trigger takes the data rate from 75
630 kHz to 6.5 kHz with 75 ms to make a decision on each event. In this time they must take
631 1600 parallel fragments, held in 150 readout systems. These fragments must be merged into
632 a single event which is a computationally slow process.

633 The Event Filter(EF) is the most comprehensive trigger and looks at the entire event as
634 reconstructed by the event builder to decide if an event will get saved to the ATLAS tier0
635 data storage center. The EF is comprised of 1800 PCs that can be interchanged with the
636 L2 PCs. The EF goes from an input data rate of 6.5 kHz to around 1 kHz output with 4
637 seconds to make a decision on each event.

638 3.3 Trigger Chains

639 A look at the final state of interest will inform what trigger chains are worth looking into.
640 For tZ the final state of interest in Figure 1.6 has the Z -boson decaying into two leptons;
641 the top-quark decaying to one lepton, one b-jet, and E_T^{miss} ; and one additional forward
642 jet. This creates a situation where many different trigger chains can be utilized effectively.
643 Despite many triggers being used the requirements by the top group and the cuts on this
644 analysis limit the practical list down to a few lepton triggers. The TOPQ2 samples have a
645 requirement that there either be ≥ 2 leptons with $pT > 15 \text{ GeV}$ and $|eta| < 2.5$ OR \geq
646 2 leptons $pT > 10 \text{ GeV}$ and ≥ 1 with $pT > 20 \text{ GeV}$ and $|eta| < 2.5$. This requirement

647 along with the lepton trigger matching requirement described in Chapter 5 and the electron
648 or muon selection described in Chapter 6 mean that the electron and muon trigger chains
649 are the most relevant. The diversity of objects in tZ means that these triggers could have
650 been relevant but they are filtered out at later levels of analysis as described in the offline
651 reconstruction section in Chapter 5.

652 **3.3.1 Single Muon**

653 Another relevant trigger that applies to this analysis is the single muon trigger. This begins
654 with the muon interacting with the various components of the detector as described in
655 Chapter 2. The most useful interaction for muon triggering purposes is the Resistive Plate
656 Chamber(RPC) hits. If there are coincident hits in multiple layers of the RPC a muon
657 candidate is flagged and passed to the HLT for the Region of Interest Builder(RoIB) can
658 create a Region of Interest(RoI). The HLT then uses this RoI to make a few requirements
659 on the quality of possible muon candidates. One of the requirements of the HLT is that hits
660 in the RPC, TGC, MDT, and ID line up in $\eta - \phi$ for a muon candidate. Another is that the
661 muons be isolated from hadronic activity to improve the selection of muons originating from
662 W -boson or Z -boson decays while mitigating muons from pion or heavy quark decays which
663 are put into B-physics streams. Cosmic muons are also rejected by tracing back where the
664 muon hits will not point back to the interaction point. Once those requirements have been
665 met further checks are performed to ensure the quality of muons that are wholly reconstructed
666 by every layer of the detector and to verify that the requirements were accurately met. The
667 event is then stored with information on the various triggers passed or failed, and objects
668 are reconstructed offline in the top derivation framework to be analyzed. [68]

669 **3.3.2 Single Electron**

670 One of the most relevant triggers that applies to this analysis is the single electron trigger.
671 This begins with the electron interacting with the various components of the detector as
672 described in Chapter 2. At L1 energy depositions in the electromagnetic and hadronic
673 calorimeters are considered, and a Region of Interest(RoI) is build around high depositions.
674 This RoI cluster must be high enough energy as well as being isolated from other activity in
675 the electromagnetic calorimeter and be isolated activity in the hadronic calorimeter. At this
676 point an EM object is passed to the HLT. Note that the object passed is not an electron yet,
677 because photons exhibit very similar behavior with its interactions in the electromagnetic
678 calorimeter. Once an RoI has been passed to the HLT we can take ID interactions into
679 account. Energy clusters in the electromagnetic calorimeter can be matched in $\eta - \phi$ and its
680 energy can be compared to the momentum measured by the inner detector tracks. Isolation
681 requirements in the electromagnetic calorimeter and hadronic calorimeter can be re-assessed
682 after corrections can be applied, and isolation on tracks can be applied to ensure the entire
683 energy deposit came from one primary vertex. Once these requirements are met the event
684 is stored with information on the various triggers passed or failed and the electron (and
685 other objects in the event) are reconstructed offline in the top derivation framework to be
686 analyzed. [68]

687 Other multilepton triggers can also contribute which work on similar principles as the
688 single electron and single muon triggers. These trigger chains have varied thresholds to
689 accept pairs of objects that are individually more loosely defined (both in energy/momentum
690 thresholds as well as isolation) compared to their single counterparts. [69]

691 Chapter 4

692 Event Simulation

693 The ability to discover anything in high energy physics hinges on our ability to accurately
694 model our backgrounds and distinguish the kinematics of these background events from the
695 kinematics of the signal being searched for. This simulation comes in three steps. First we
696 simulate the parton level interactions. Then we go through parton showering process to take
697 the bare quarks and hadronize them into jets. Finally we go through detector simulation in
698 order to mimic how real data will look in ATLAS.

699 4.1 The Monte Carlo Method

700 Simulating data begins with the standard model predictions which in principle can be cal-
701 culated exactly. In principle we employ the monte carlo method to perform integrations
702 that are cumbersome to perform by hand and where numerical methods are more appro-
703 priate. There are a plethora of generators which excell at simulating various processes. To
704 decide between the various generators consulting previous work within the single top group
705 was helpful. Recomendations were used for every sample except tZ for which there was no
706 reccomendation. The reccomendations were as follows.

707 4.2 Signal Simulation

708 Several Monte Carlo generators were considered to model the tZ process. Madgraph and
709 POWHEG-box were used to generate samples and compare them while MCFM was used to
710 calculate NLO cross-sections to scale the LO Madgraph samples. Madgraph5+Pythia8 was
711 chosen to use the same generator as $t\bar{t}+X$. Another reason Madgraph5+Pythia8 was chosen
712 was that Madgraph and Pythia have been widely used tools for quite a while in high energy
713 physics and as a result are very well understood generators with good simulation of a wide
714 variety of physics processes.

715 The sample was simulated with the Z -boson decaying into two leptons and the top-quark
716 decaying to one lepton, one b -jet, and E_T^{miss} . This guides which backgrounds are necessary
717 to simulate as well as which data triggers needed to be considered.

718 4.3 Diboson

719 Among the most prominent backgrounds is diboson which is a large non-top background in
720 this analysis. Its relative contribution is not suprising considering the most promenent dibo-
721 son contribution is WZ which contains a real Z -boson, three leptons, and MET. Aditional
722 jets can come from Initial State Radiation (ISR) or Final State Radiation (FSR). Diboson
723 was modeled with Powheg and showered in Pythia6.

724 4.4 $t\bar{t}$

725 $t\bar{t}$ is a dominant background for almost any search involving a top quark. Its large cross
726 section means that it is dificult to remove even if distinct kinematic differences exist. $t\bar{t}$ can

727 have 0, 1, or 2 leptons, meaning that every $t\bar{t}$ event that passes selection by definition has
728 a fake lepton. Beyond having a fake lepton two of those lepton will have to fake a Z -boson
729 within the constraints outlined in Chapter 6. $t\bar{t}$ was modeled with Powheg and showered
730 with Pythia6.

731 **4.5 $t\bar{t}+X$**

732 $t\bar{t}+X$ is a process that has been under study by the single top group within ATLAS and
733 has been showing promising gains *source*. $t\bar{t}+Z$ contributes much more strongly when
734 compared with $t\bar{t}+W$ due to the real Z -boson. This process has 0, 1, 2, 3, or 4 real leptons,
735 and only the 3 lepton contribution contributes to our final state as selection cuts in Chapter 6
736 describe. $t\bar{t}+X$ is modeled by Madgraph5 and showered with Pythia8.

737 **4.6 Z -boson+jets**

738 Z -boson+jets is another large background sporting a real Z -boson, but despite not having
739 a top quark and only having two real leptons, it still remains an important background to
740 consider due to its large cross section. Z -boson+jets taken in combination with $t\bar{t}$ constitutes
741 a majority of fakes that come up in this analysis due to these samples naturally containing
742 fewer than three leptons. Z -boson+jets was modeled and showered with Sherpa.

743 **4.7 Single top-quark**

744 Of paramount interest to the single top group is single top-quark production. t -channel and
745 s -channel both have only one lepton, and while considered for this analysis, they contribute

746 no events to the event yield. Wt -channel however has two real leptons and a real top quark
747 which leaves it close enough to tZ to add to the event yield in a small way. Single top-quark
748 simulation was performed with Powheg+Pythia8.

749 4.8 W -boson+jets and Multijet

750 Also considered for this analysis is W -boson+jets production. This process, despite having an
751 immense cross section in comparison to other background considered, was completely eliminated
752 by preselection cuts described in Chapter 6 because it has no Z -boson, only one lepton
753 so it would require 2 fake leptons, and has no top-quark. Given that this process has
754 no contribution due to the combinatorics of requiring so many fake leptons and bosons
755 multijets will also have no contribution as it would require three fake leptons that would
756 also be required to match the kinematics of the W -boson and Z -boson. Both Sherpa and
757 Powheg+Pythia were considered for W +jets simulations.

758 **Chapter 5**

759 **Object & Event Reconstruction**

760 High energy physics is messy. Having particles that interact with several different layers of
761 the detector makes our particle identification and reconstruction complex but possible. By
762 using tracking from the inner detector, energy measurements from the calorimeters, more
763 tracking from the muon spectrometers, and by looking at global variables that have to do
764 with event kinematics we can ensure quality physics objects for analysis. This analysis in
765 particular uses a wide variety of objects including electrons, muons, light jets, heavy jets,
766 E_T^{miss} , reconstructed W -bosons and Z -bosons, and the heaviest of all fundamental particles
767 with one of the most unique signatures, the top quark.

768 **5.1 Electron Reconstruction**

769 Electrons use information from the inner detector and the electromagnetic calorimeter. Elec-
770 trons are among the more scrutinized reconstructed objects because hadronic jets, photons,
771 and taus can fake electrons heightening the importance of quality control. To achieve this
772 electron candidates are required to be within $|\eta| < 2.47$ as measured by the tracks in the
773 ID with $p_T > 7 \text{ GeV}$ as measured by the calorimeter. Requirements on the transverse impact
774 parameter (d_0) and the longitudinal impact parameter (z_0) constrain the degree to which
775 tracks in the ID are allowed to vary from the interaction point while still being counted as
776 part of the electron object. Ratios of energy measured in the electromagnetic calorimeter

777 and the hadronic calorimeter are also used to reject jets that interact with the electromag-
778 netic calorimeter and could fake electrons. Ratios of energy in varying window sizes in the
779 electromagnetic calorimeter are also used to help distinguish other activity such as pions
780 from electrons. These reconstructed electrons are then trigger matched with L1 EM objects
781 and HLT electrons [70] [71] [72].

782 5.2 Muon Reconstruction

783 Muons can use information from the inner detector, the muon systems, and to a lesser
784 extent the calorimeters. Muons are not stopped by the detector making full calorimetry
785 impossible so their energy must be determined by their curvature in the magnetic field set
786 up by ATLAS’s namesake toroidal magnet system.

787 There are four algorithms that are used in muon reconstruction and define the tightness
788 of the muons provided to analyzers. The Moore algorithm/Muid standalone method starts
789 from hits in the muon spectrometer and traces them back to a primary vertex to create a
790 standalone muon. The Muid Combined method combines an inner detector track with a
791 muon spectrometer track to produce a combined muon. The MuGirl method performs a
792 search for segments and tracks in the muon spectrometer using an inner detector track as a
793 seed. If the refit performed by the MuGirl method is successful a Combined muon is made,
794 if not then a tagged muon is made. The fourth is the MuTagIMO method which identifies
795 muons by associating an inner detector track with a standalone muon in a similar way as
796 the Moore/Muid standalone method to produce a tagged muon. Muons from all of these
797 algorithms are added after overlapping definitions are accounted for.

798 The tightness of the muon is defined based on which of the four algorithms have been

799 successful in constructing the muon. A tight muon is one where the Muid combined and
800 MuGirl muons have been successfully combined. A medium muon includes all standalone
801 muons. Loose muons are all muons found by tagging algorithms and have an inner detector
802 track with silicon hits associated with it. Lastly a very loose muon includes MuTagIMO
803 muons which are allowed to not have any silicon hits, but have TRT only tracks in the inner
804 detector [73] [74].

805 5.3 Jet Reconstruction

806 Hadronizing quarks and gluons interact with the inner tracker, the electromagnetic calorime-
807 ter, and the hadronic calorimeter. We use this information to reconstruct the location and
808 energy of the jets.

809 There are several jet reconstruction algorithms but the most common are described by
810 equations 5.1 and 5.2

$$d_{ij} = \min(p_{T,i}^{2p}, p_{T,j}^{2p}) \frac{\Delta\eta_{ij}^2 + \Delta\phi_{ij}^2}{R^2} \quad (5.1)$$

$$d_i = p_T^{2p} \quad (5.2)$$

811 where the exponent p is either 1, 0, or -1 which correspond to the kt, Cambridge Achen,
812 or anti-kt algorithm [75]. These algorithms work by considering every cell of the detector as
813 an object in a list enumerated by i and j and considering pairs of these cells for combination
814 by this equation. If the minimum d_{ij} is smaller than d_i then the two objects are combined
815 into one object. If a d_i is smaller then that object is removed and considered a jet. This

816 continues until all objects are removed from the list. The parameter R sets the separation
817 distance between two jets.

818 The first of these three algorithms is the kt algorithm which gives irregular jets, but is
819 more theoretically sound than simple cone drawing. The Cambridge Aachen algorithm gives
820 jets that are slightly more regular but are larger than their kt counterparts, while the anti-kt
821 algorithm gives jets that are more regular than the kt. This is the algorithm of choice for
822 ATLAS and this analysis considers anti-kt jets with an R parameter of 0.4.

823 After the selection of jets with the anti-kt algorithm corrections are applied to each jet
824 based on the jet's position and p_t to correct for specific detector effects. These corrected jets
825 have a series of quality cuts applied including a check for unphysical negative energy jets
826 and electron isolation requirements to ensure that an electron is not being double counted
827 as a jet.

828 5.3.1 Jet b -tagging

829 b-jets are unique because the b quark decays after the hadronization process begins but
830 before it interacts with the detector. This creates a secondary vertex (displaced by a few
831 millimeters) which can be found by looking at the tracking information from the inner
832 detector. This is the heart of b -tagging algorithms used in ATLAS. The b -tagging algorithm
833 used in ATLAS for run 2 is the MV2c20 algorithm. When this algorithm is applied to
834 anti-kt jets with an R parameter of 0.4 the p_t of the jet is required to be greater than
835 20GeV, the η is required to be less than 2.5, and for high p_T jets (greater than 50GeV) the
836 Jet Vertex Tagger (JVT) output variable is required to be greater than 0.64. The MV2c20
837 algorithm is a neural network analysis of b -tagging algorithms used in ATLAS to create a
838 single discriminating variable that can distinguish between jets originating from a b-quark

839 and all other jets. [76].

840 5.4 Z boson

841 Now that we have the leptons defined we can reconstruct the intermediate Z boson. To do
842 this we require that the Z -boson be constructed from an Opposite-Sign Same-Flavor (OSSF)
843 lepton pair. With three leptons (which can be electrons or muons) we can have 1, 2, or 0
844 OSSF pairs. These are two fundamental cuts we make in Section 6.1. When there is one OSSF
845 pair the Z -boson is reconstructed with those, and the remaining lepton is used to reconstruct
846 the W -boson. When there are two OSSF pairs then the OSSF pair which reconstructs the Z -
847 boson mass more closely is considered, and the remaining lepton reconstructs the W -boson.
848 The last case with no OSSF pair represents either a charge misidentification of a lepton or
849 a fake lepton whose charge couldn't be properly reconstructed. In this case the event is
850 rejected.

851 5.5 Missing Transverse Energy and the W -boson

852 For each event we apply conservation of momentum in the transverse plane of the detector
853 to obtain what is known as missing transverse energy (E_T^{miss}). E_T^{miss} is commonly used as a
854 stand in for some information on neutrinos. While we can not apply the same method to find
855 the neutrino p_z , because the colliding partons do not necessarily have balanced z momenta,
856 we can make the assumption that it came from a W -boson and begin with conservation of
857 momentum of the W -boson decay vertex.

$$p_w^\mu = p_\nu^\mu + p_l^\mu \tag{5.3}$$

858 The lepton up for consideration is the one that did not come from the Z -boson. Solving
 859 for the p_z of the neutrino we come to the following quadratic.

$$p_{z\nu} = \frac{\alpha p_{zl}}{p_{tl}^2} \pm \sqrt{\frac{\alpha^2 p_{zl}^2}{p_{tl}^4} - \frac{E_l^2 p_{t\nu}^2 - \alpha^2}{p_{tl}^2}} \quad (5.4)$$

$$\alpha = \frac{m_w^2}{2} + \cos(\Delta\phi)p_{t\nu}p_{tl} \quad (5.5)$$

860 Equation 5.4 can have two, one, or no real solutions. If it has two real solutions the one
 861 with lower p_z is chosen. In the case where there are no real solutions the measured E_T^{miss} is
 862 scaled to the point where one real solution is found. The measured E_T^{miss} and azimuthal angle
 863 (ϕ) of the E_T^{miss} and the reconstructed p_z , along with the fact that neutrinos are functionally
 864 massless, define the neutrino four vector.

865 Now that the neutrino is defined we have reconstructed the four vectors for all of our
 866 final state particles. We can reconstruct the W -boson, but the mass will already be defined
 867 because we assumed the W -boson mass in reconstructing the neutrino. For this reason
 868 the experimental variable m_T^W , which is the transverse mass of the W -boson, is defined in
 869 equation 5.6. It is used to help distinguish events that have a real W -boson from events that
 870 don't [77].

$$m_{tw}^2 = 2E_{Tl}E_{Tv}(1 - \cos(\Delta\phi)) \quad (5.6)$$

871 **5.6 Reconstructing the top-quark**

872 Once the W -boson is reconstructed, and the b-jet selected the reconstruction of the top-
873 quark is simply the result of the addition of the four vectors of the two. The top-quark
874 decay has properties that are used to help distinguish signal and backgrounds even though
875 this analysis has significant top-quark backgrounds as seen in Chapter 6.

876 **Chapter 6**

877 **Analysis**

878 After the Z -boson, the top-quark, the W -boson from the top-quark decay, and the neutrino
879 from the W -decay are reconstructed as described in Chapter 5 they were used to help separate
880 tZ from the various backgrounds. The energies and positions of each of these objects in our
881 detector, as well as the multiplicity of the objects, was used to achieve this separation. The
882 decisions made in the preselection and cut flow were informed by the kinematics of the
883 tZ process. The tZ Feynman diagram is shown in Figure 1.6.

884 **6.1 Preselection**

885 One goal in setting up an analysis is to understand the background model in relation to the
886 observed data. To accomplish this defining characteristics of the signal region were determined
887 in order to limit the number of monte carlo samples needed. Because the signal has three
888 leptons and a Z -boson, cuts on the number of leptons and Z -mass (for instance) were applied
889 to limit any contribution from certain low lepton multiplicity non Z -boson sources (W -
890 boson+jets, multijets, etc...).

891 The following cuts were optimized to improve agreement between data and the back-
892 ground model while maintaining as much signal statistics as possible.

- 893 • Exactly 3 leptons with $p_T > 10\text{GeV}$.
- 894 • At least one OSSF pair.

- 895 • $80\text{GeV} < \text{Z mass} < 100\text{GeV}$. Figure 6.3
- 896 • Leading lepton $p_T > 40\text{ GeV}$. Figure 6.1
- 897 • Second lepton $p_T > 20\text{GeV}$. Figure 6.1
- 898 • Third lepton $p_T > 10\text{GeV}$. Figure 6.1
- 899 • 2, 3, or 4 jets with $p_T > 25\text{GeV}$. Figure 6.2
- 900 • Leading jet $p_T > 40\text{GeV}$. Figure 6.2
- 901 • Exactly 1 b-jet at 85% WP. Figure 6.2
- 902 • MET $> 20\text{GeV}$. If the Transverse $< 40\text{GeV}$ then MET $> 40\text{GeV}$ is required. Fig-
- 903 ure 6.3 Figure 6.3

904 **6.2 Control Regions**

905 here i need to add Z+jets control region and ttbar control region descriptions and histograms

906 **6.3 Cut Flow**

907 Once the preselection region is defined our goal is to improve the sensitivity of the analysis.

908 We do this by searching for variables where the shape of the signal significantly differs from

909 the shape of one or all of the backgrounds and evaluating its effect on the value S/\sqrt{B} .

910 S/\sqrt{B} is used as the variable to optimize because it ensures both strong signal to back-

911 ground ratios while also ensuring that we limit the contribution of statistical errors. Many

912 distributions were considered for various reasons, but distributions of special interest are

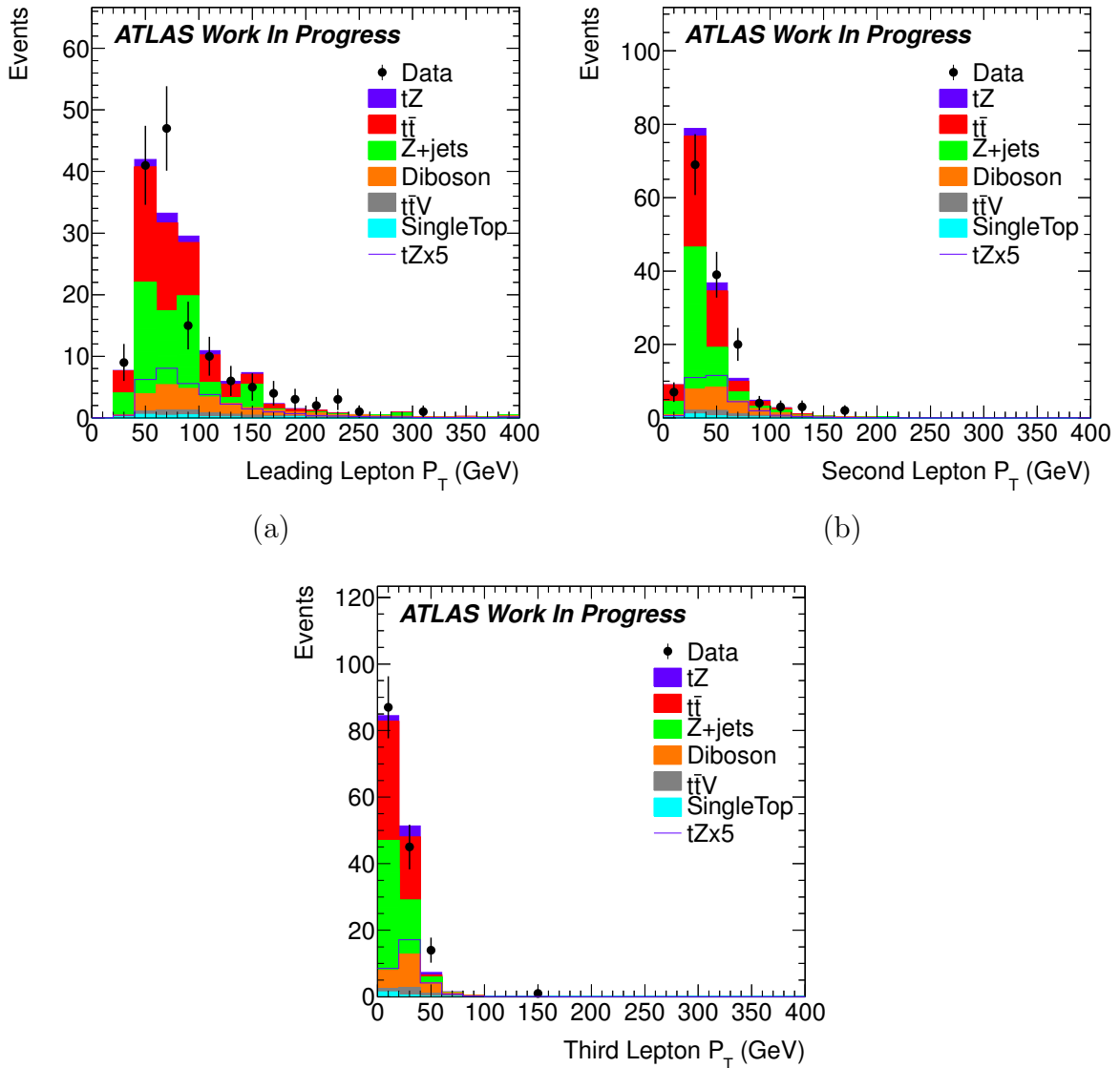


Figure 6.1: Lepton p_T for leading (a), second (b), and third (c) leptons with preselection applied except the cuts on the variable shown.

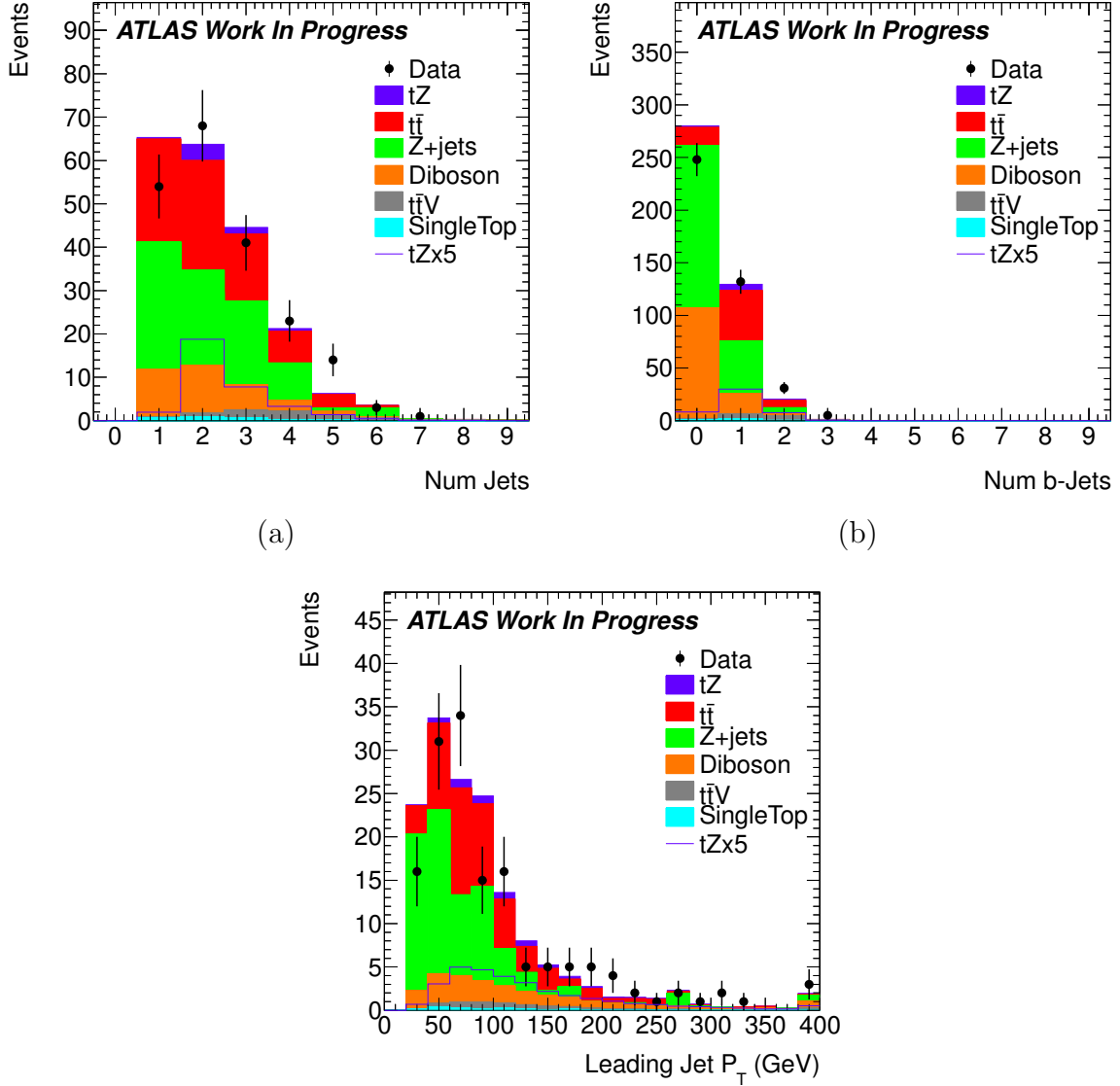


Figure 6.2: Number of jets (a), number of b-jets (b), and p_T of the leading jet (c) with preselection applied except the cuts on the variable shown. At least one jet was required at this level.

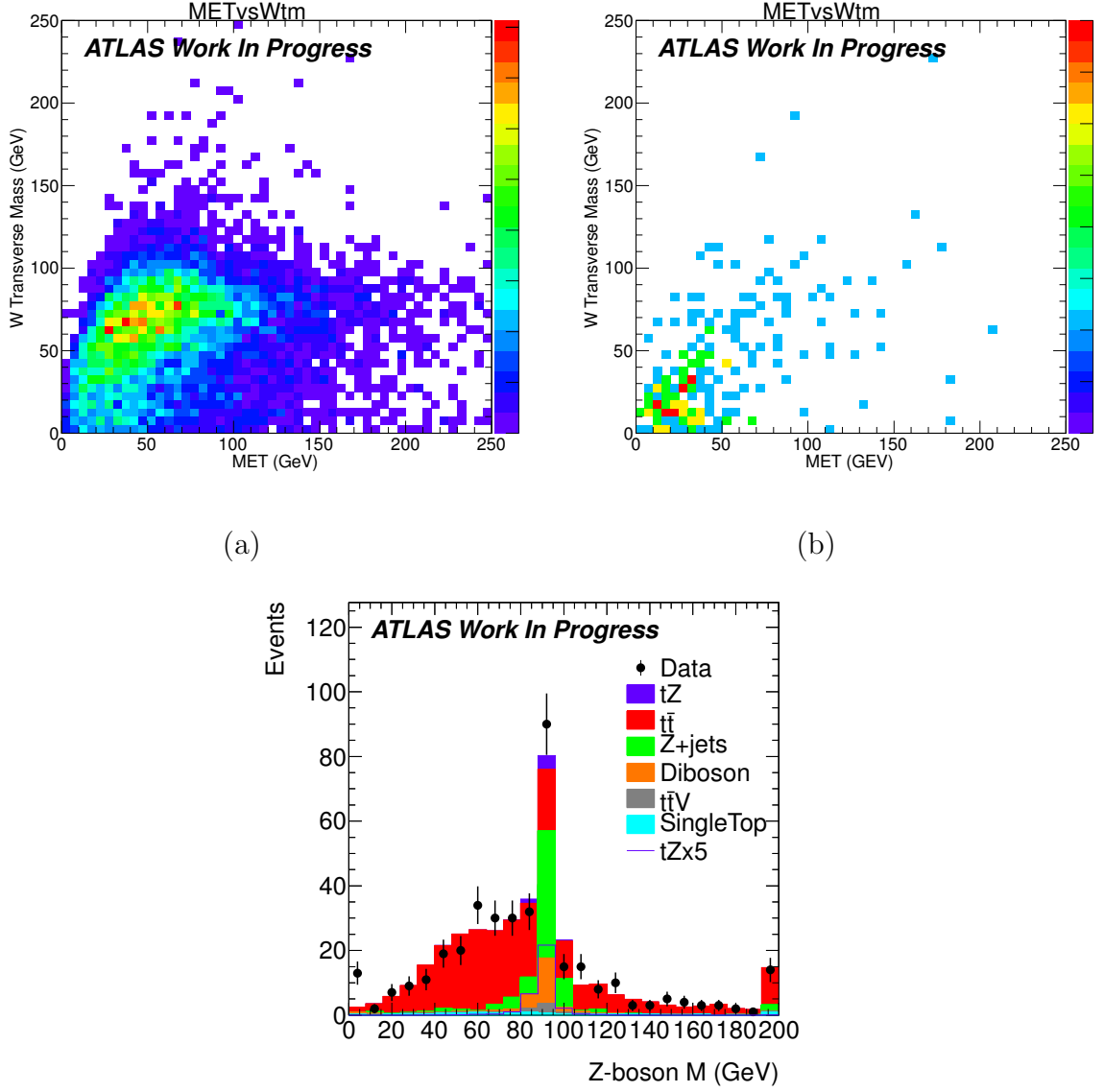


Figure 6.3: Further histograms with preselection applied except the cuts on the variable shown. Invariant mass of the Z -boson (c), two dimensional map of transverse mass of the W -boson vs MET for the signal (a), and two dimensional map of transverse mass of the W -boson vs MET for the data (b).

913 the angular variables and top-quark mass shown in Figure 6.10. The distributions with the
 914 best discriminating power are used for this analysis and the degree to which each of these
 915 cuts improve S/\sqrt{B} is shown in Table 6.1. Those are the W -boson transverse mass, the
 916 η value of the leading non b-jet, and the angle between the b-jet and the leading non b-jet
 917 shown in Figure 6.5. Those variables were then re-optimized sequentially to show that any
 918 correlations were minor, and to ensure optimal sensitivity.

Process	Preselection	Wtm cut applied	LeadNonBjetEta cut applied	full selection
$t\bar{t}$	104.03	28.12	14.96	10.39
single top-quark	3.58	1.03	0.49	0.34
tV	0.92	3.12	1.03	0.61
$Z + \text{jets}$	186.45	5.33	2.30	1.75
Diboson	14.91	12.85	5.18	3.30
tZ	3.30	4.26	3.22	2.89
Total Expected	313.19	54.70	27.19	19.28
Data Observed	272.00	62.00	29.00	22.00
S/B	0.01	0.08	0.13	0.18
S/sqrtB	0.19	0.60	0.66	0.71

Table 6.1: Event yields after various stages of analysis.

919 Once we have applied the full cut flow we are left with the remaining distributions to
 920 analyze. These are meant to represent the kinematics of events selected by this analysis.
 921 The application of the full selection takes us from having approximately one signal event in
 922 100 to nearly 1 signal event in 5. These efforts will greatly improve the sensitivity of our
 923 analysis as shown in the next chapter.

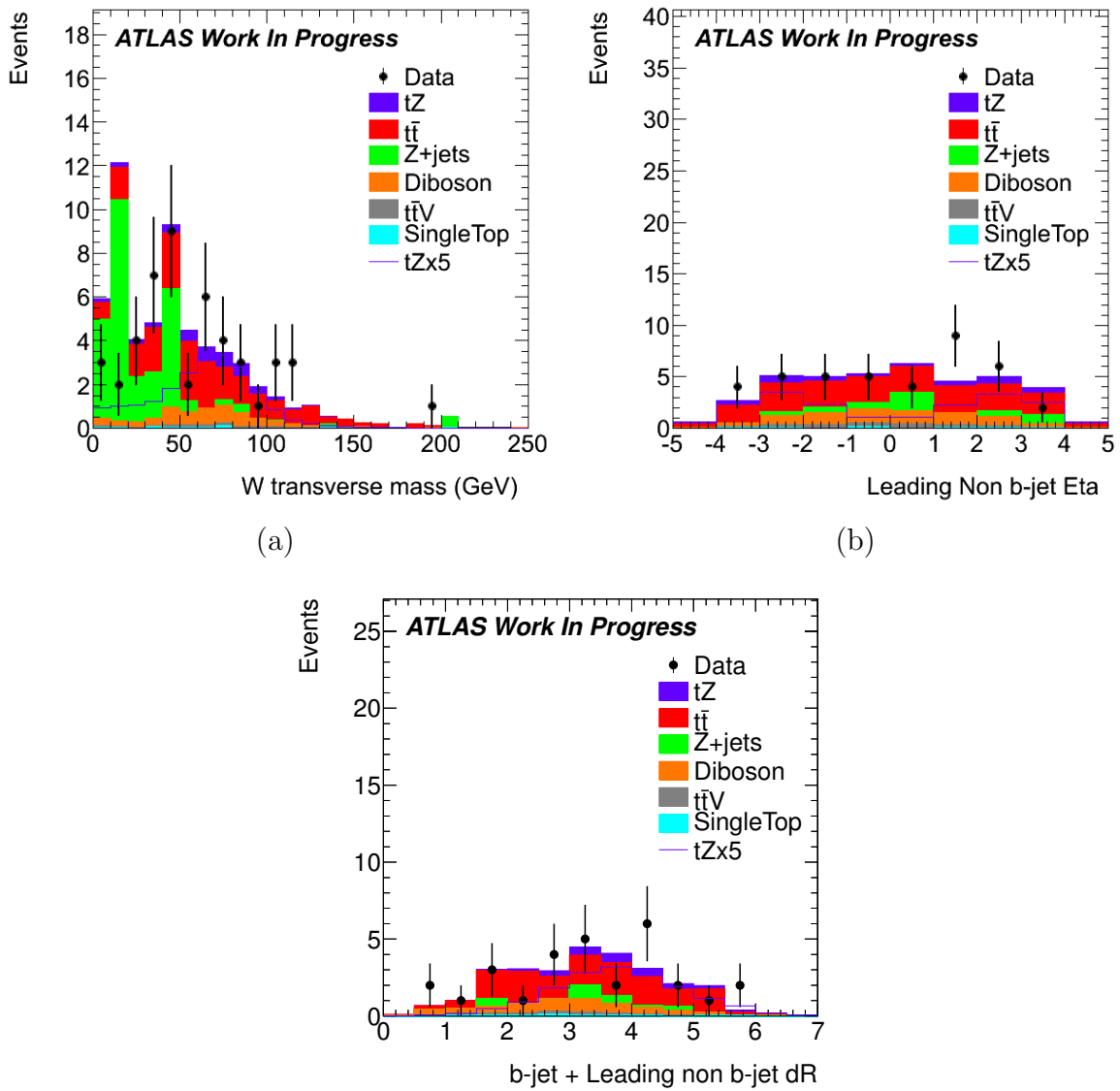


Figure 6.4: Variables with full selection applied except the cut on this variable.

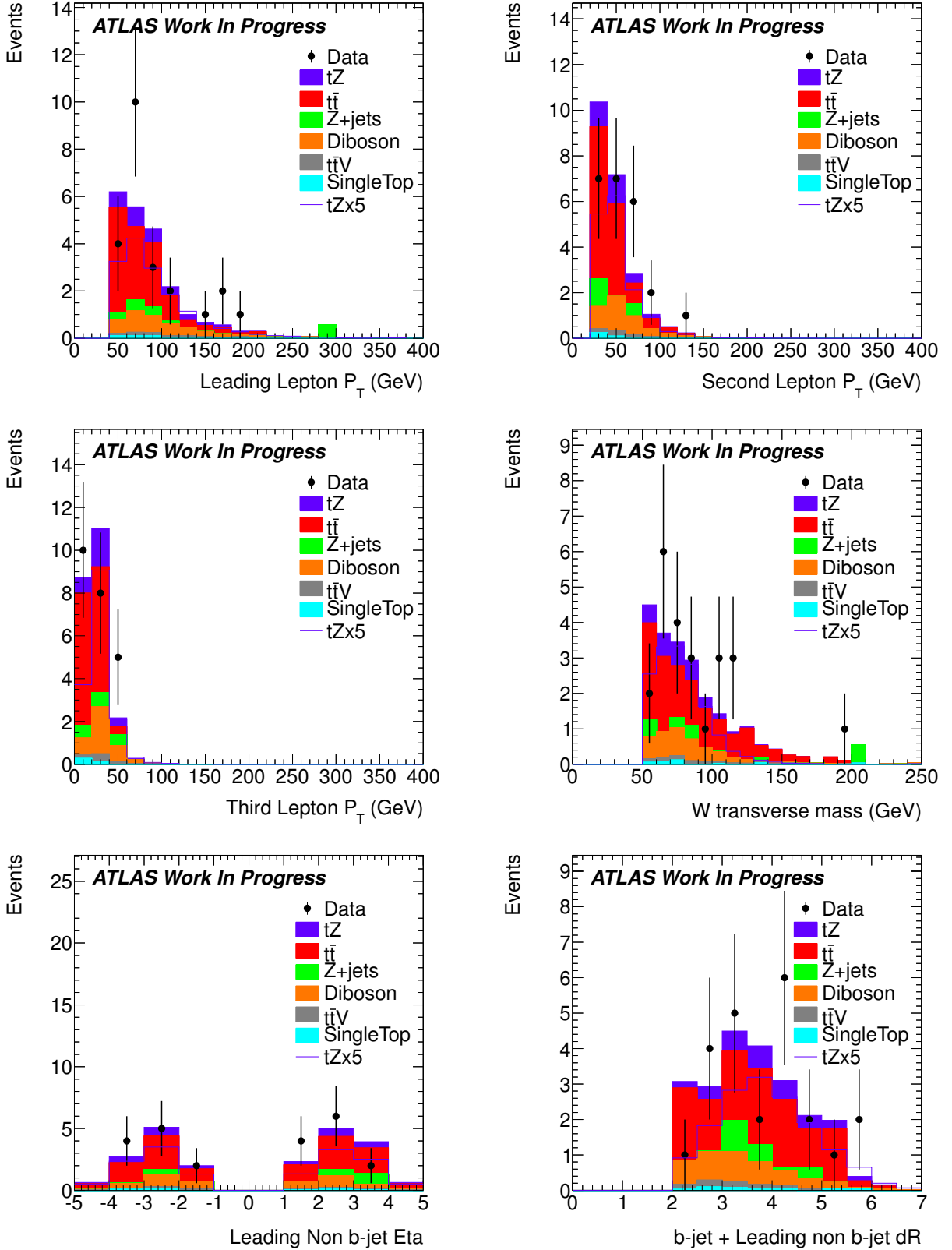


Figure 6.5: Lepton p_T for leading, second, and third leptons with full selection applied as well as histograms of the three cuts made to finalize selection with full selection applied.

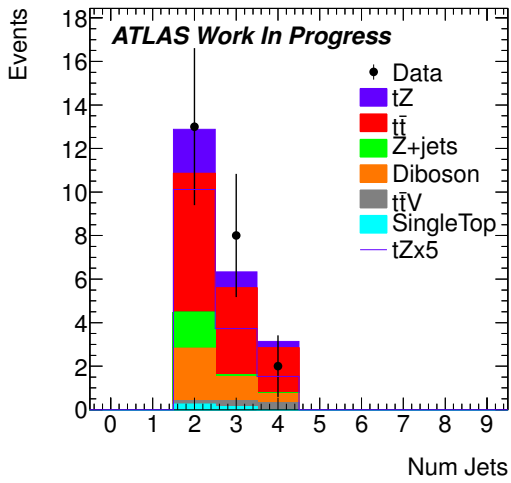


Figure 6.6: Number of jets with full selection applied.

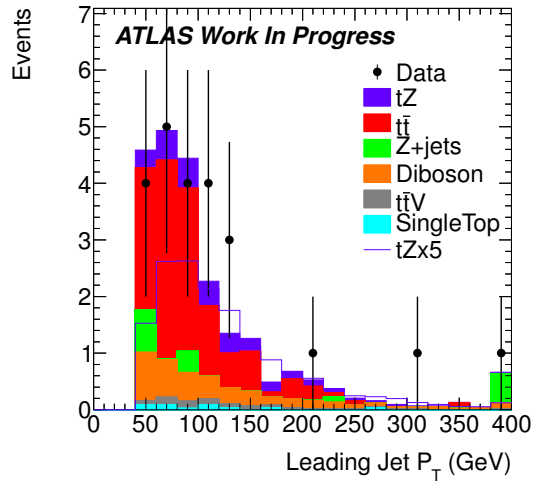


Figure 6.7: Leading Jet P_T with full selection applied.

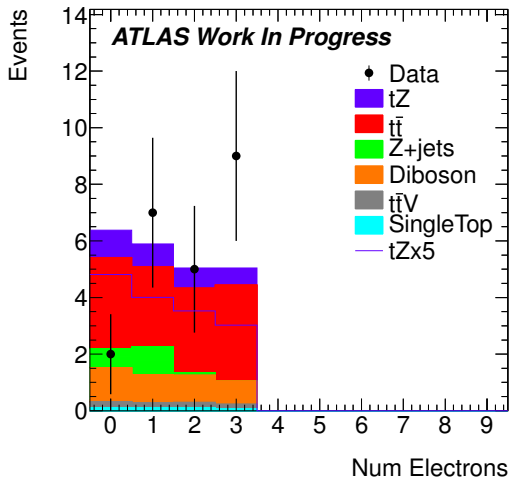


Figure 6.8: Histograms of number of electrons. Note that because we require three leptons exactly these histograms are mirrors of each other by definition.

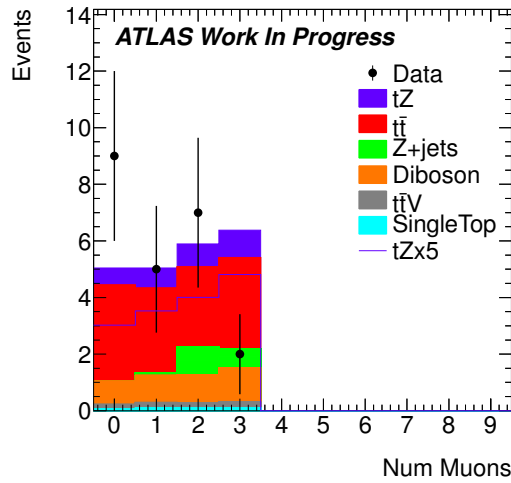


Figure 6.9: Histograms of number of muons. Note that because we require three leptons exactly these histograms are mirrors of each other by definition.

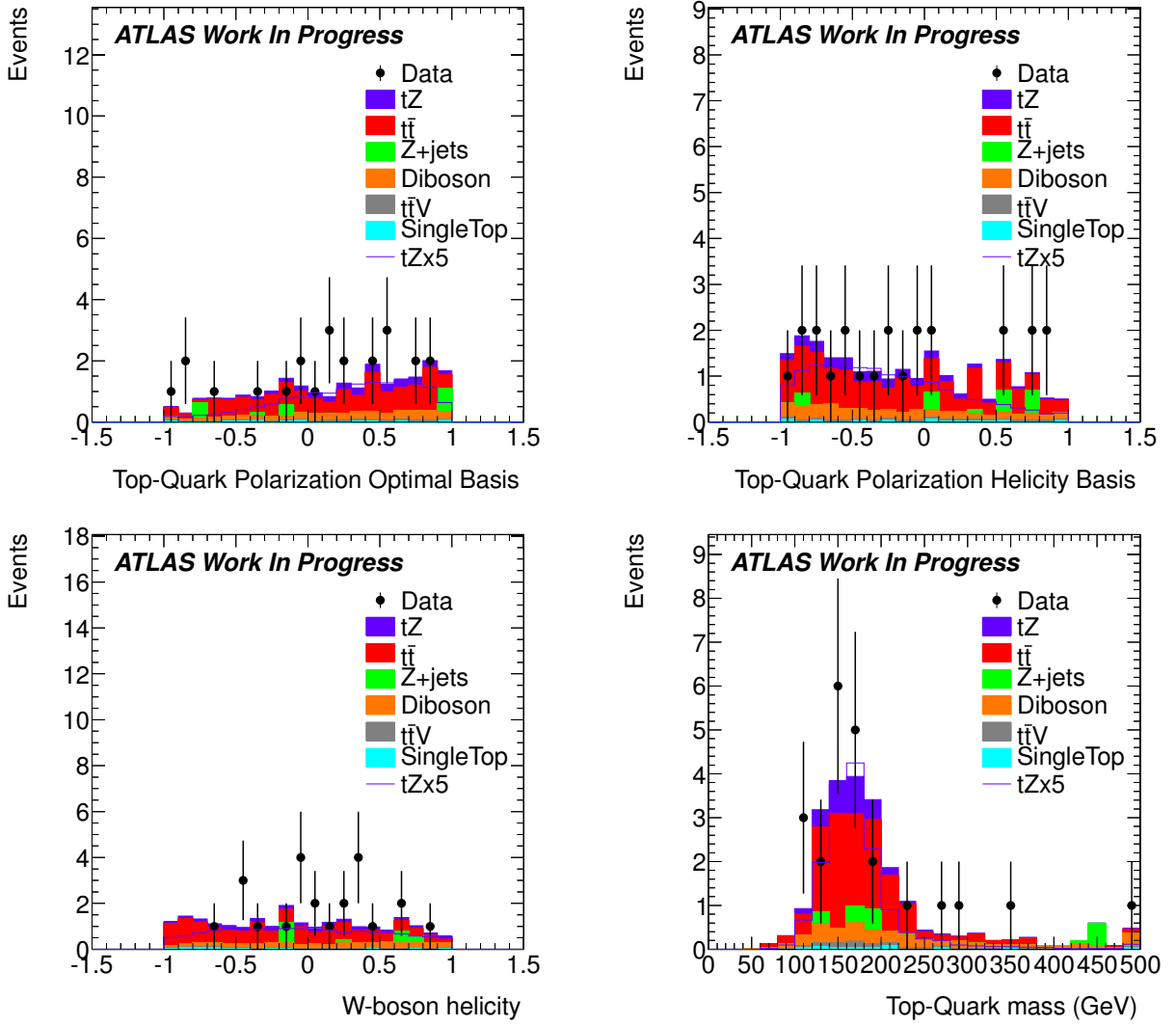


Figure 6.10: Variables which display properties of the top quark and its decay with full selection applied.

924 **Chapter 7**

925 **Results**

926 statistics likelihood and more functions hcpss stats talks

927 Bayesian address the question everyone is interested in by using assumptions no one
928 believes. Frequentest use impeccable logic to deal with an issue of no interest to anyone.

929 -L.Lyons

930 cookies are good...

931 **7.1 Systematic Uncertainties**

932 **7.2 Statistical Analysis**

933 **7.3 Conclusions**

934 **7.4 more citations**

935 This section is just my notes for where some more useful citation are.

936 TOPCOMMONOBJECTS [78]

937 TOPMET [79]

938 JES [80] [81]

939 ATLAS-LUMI [9]

- 940 ROOSTAT [82]
941 JETUNCERTAINTIES [83]
942 LUMIPLOTS [46]
943 TOPCOMMONSYSTEMATICS [84]
944 JESUNCERTAINTYSOFTWARE [85]
945 JRE [86]
946 ELECTRONENERGYSYSTEMATICS [87]
947 MUONENERGYSYSTEMATICS [88]
948 TOPMET [79]
949 PLRcite [89]
950 ProfileWiki [90]
951 KS [91]
952 ProfileLikelihoodUncertainty [92]
953 BAT [93]

BIBLIOGRAPHY

BIBLIOGRAPHY

- 955 [1] N. Kidonakis, *Top quark pair and single top production at Tevatron and LHC*
956 energies, July, 2010.
- 957 [2] P. Kant, O. M. Kind, T. Kintscher, T. Lohse, T. Martini, S. Mlbitz, P. Rieck, and
958 P. Uwer, *HatHor for single top-quark production: Updated predictions and uncertainty*
959 *estimates for single top-quark production in hadronic collisions*, Comput. Phys.
960 Commun. **191** (2015) 74–89, arXiv:1406.4403 [hep-ph].
- 961 [3] T. E. online, *The Standard Model of high energy physics Years from concept to*
962 *discovery*, July, 2012.
- 963 [4] A. Heinson, *Feynmann Diagrams for Top Physics Talks and Notes*, Oct, 2011.
- 964 [5] D. Binosi and L. Theul, *JaxoDraw: A graphical user interface for drawing Feynman*
965 *diagrams*, Computer Physics Communications **161** (2004) no. 1-2, 76 – 86.
966 <http://www.sciencedirect.com/science/article/pii/S0010465504002115>.
- 967 [6] J. Campbell, R. K. Ellis, and R. Ronisch, *Single top production in association with a*
968 *Z boson at the LHC*, Phys.Rev. **D87** (2013) 114006, arXiv:1302.3856 [hep-ph].
- 969 [7] A. Horvath, *The LHC experiments and the preaccelerators.*, Nov, 2009.
- 970 [8] M. Brice, *First LHC magnets installed. Installation du premier aimant du LHC*, Apr,
971 2005.
- 972 [9] ATLAS Collaboration, *Updated Luminosity Determination in pp Collisions at*
973 $\sqrt{s} = 7 \text{ TeV}$ *using the ATLAS Detector*, ATLAS-CONF-2011-011 (2011) .
- 974 [10] M. Brice, *Installing the ATLAS calorimeter*, Nov, 2005.
- 975 [11] J. Pequenao and P. Schaffner, *An computer generated image representing how ATLAS*
976 *detects particles*, Jan, 2013.
- 977 [12] J. Pequenao, *Computer generated image of the whole ATLAS detector*, Mar, 2008.

- 978 [13] ATLAS Collaboration, *The ATLAS Experiment at the CERN Large Hadron Collider*,
 979 JINST **3** (2008) S08003.
- 980 [14] A. Salzburger, *The ATLAS Track Extrapolation Package*, Dec, 2007.
- 981 [15] C. A. M. M. Brice, *Preparation for the lowering of the second Magnet End Cap Toroid*
 982 *into ATLAS cavern side C*, Jul, 2007.
- 983 [16] J. Pequenao, *Computer generated image of the ATLAS inner detector*, Mar, 2008.
- 984 [17] J. Pequenao, *Computer Generated image of the ATLAS calorimeter*, Mar, 2008.
- 985 [18] J. Pequenao, *Computer generated image of the ATLAS Muons subsystem*, Mar, 2008.
- 986 [19] C. Marcelloni, *Installation of the first of the big wheels of the ATLAS muon*
 987 *spectrometer, a thin gap chamber (TGC) wheel. Installation de la premire des grandes*
 988 *roues du ATLAS spectromtre muons, une roue TGC*, Sep, 2006.
- 989 [20] D. Griffiths, *Introduction to Elementary Particles*. Wiley-VCH Verlag GmbH & Co.
 990 KGaA, Weinheim, 2004.
- 991 [21] M. E. Peskin and D. V. Schroeder, *An Introduction to Quantum Field Theory*.
 992 Westview Press, 1995.
- 993 [22] C. Itzykson and J.-B. Zuber, *Quantum Field Theory*. McGraw-Hill, 1980.
- 994 [23] ATLAS Collaboration, G. Aad et al., *Observation of a new particle in the search for*
 995 *the Standard Model Higgs boson with the ATLAS detector at the LHC*, Phys. Lett.
 996 **B716** (2012) 1–29, arXiv:1207.7214 [hep-ex].
- 997 [24] J. A. Gallian, *Contemporary Abstract Algebra*. Houghton Mifflin Company, 2002.
- 998 [25] W.-K. Tung, *Group Theory in Physics*. World Scientific Publishing Co. Pte. Ltd.,
 999 1985.
- 1000 [26] T.M. Liss, F. Maltoni, and A. Quadt, *The Top Quark*, tech. rep., Particle Data
 1001 Group, 2015.
- 1002 [27] M. Jezabek J. Kuhn, *Top quark width: Theoretical update*, Phys. Rev. D **48** (1993) .

- ¹⁰⁰³ [28] CDF Collaboration, *Direct Top-Quark Width Measurement at CDF*, Physical review letters **105** (2010) no. 23, 232003.
- ¹⁰⁰⁵ [29] D0 Collaboration, *Determination of the width of the top quark*, Physical review letters **106** (2011) no. 2, 022001.
- ¹⁰⁰⁷ [30] A. Heinson, A. Belyaev, and E. Boos, *Single top quarks at the Fermilab Tevatron*, Physical Review D **56** (1997) no. 5, 3114.
- ¹⁰⁰⁹ [31] CDF Collaboration, *Observation of Top Quark Production in $\bar{p}p$ Collisions with the Collider Detector at Fermilab*, Phys. Rev. Lett. **74** (1995) 2626 – 2631.
¹⁰¹⁰ <http://link.aps.org/doi/10.1103/PhysRevLett.74.2626>.
- ¹⁰¹² [32] D0 Collaboration, *Observation of the Top Quark*, Phys. Rev. Lett. **74** (1995) 2632–2637. <http://link.aps.org/doi/10.1103/PhysRevLett.74.2632>.
- ¹⁰¹⁴ [33] D0 Collaboration, *Observation of Single Top Quark Production*, Phys.Rev.Lett. **103** (2009) 092001, [arXiv:0903.0850](https://arxiv.org/abs/0903.0850) [hep-ex].
- ¹⁰¹⁶ [34] CDF Collaboration, *First Observation of Electroweak Single Top Quark Production*, Phys.Rev.Lett. **103** (2009) 092002, [arXiv:0903.0885](https://arxiv.org/abs/0903.0885) [hep-ex].
- ¹⁰¹⁸ [35] D0 Collaboration, *Determination of the width of the top quark*, Phys. Rev. Lett. **106** (2011) 022001.
- ¹⁰²⁰ [36] F.-P. Schilling, *Top Quark Physics at the LHC: A Review of the First Two Years*, Int.J.Mod.Phys. **A27** (2012) 1230016, [arXiv:1206.4484](https://arxiv.org/abs/1206.4484) [hep-ex].
- ¹⁰²² [37] ATLAS Collaboration, *Observation of t Channel Single Top-Quark Production in pp Collisions at $\sqrt{s} = 7$ TeV with the ATLAS detector*, Tech. Rep. ATLAS-CONF-2011-088, CERN, Geneva, Jun, 2011.
- ¹⁰²⁵ [38] ATLAS Collaboration, G. Aad et al., *Evidence for the associated production of a W boson and a top quark in ATLAS at $\sqrt{s} = 7$ TeV*, Phys.Lett. **B716** (2012) 142–159, [arXiv:1205.5764](https://arxiv.org/abs/1205.5764) [hep-ex].
- ¹⁰²⁸ [39] E. Boltezar, H. Haseroth, W. Pirkl, T. Sherwood, U. Tallgren, P. Tetu, D. Warner, and M. Weiss, *The New CERN 50MeV Linac*, Proc. 1979 Linear Accelerator Conference **BNL 51134** (1979) no. 66, .

- 1031 [40] B. Mikulec, A. Blas, C. Carli, A. Findlay, K. Hanke, G. Rumolo, and J. Tan, *LHC*
 1032 *Beams from the CERN PS Booster*, .
- 1033 [41] M. e. a. Barnes, *The PS complex as proton pre-injector for the LHC: design and*
 1034 *implementation report*. CERN, Geneva, 2000.
- 1035 [42] P. Collier and B. Goddard, *PREPARATION OF THE SPS AS LHC INJECTOR*.
 1036 CERN, Geneva, 1998.
- 1037 [43] O. S. Brning, P. Collier, P. Lebrun, S. Myers, R. Ostojic, J. Poole, and P. Proudlock,
 1038 *LHC Design Report*. CERN, Geneva, 2004.
- 1039 [44] O. S. Brning, P. Collier, P. Lebrun, S. Myers, R. Ostojic, J. Poole, and P. Proudlock,
 1040 *LHC Design Report*. CERN, Geneva, 2004.
- 1041 [45] V. Papadimitriou, *Luminosity determination at the Tevatron*, LHC Lumi Days **LHC**
 1042 **Workshop on LHC Luminosity Calibration CERN-Proceedings-2011-001**
 1043 (2011) 90–95, 1106.5182:<http://arxiv.org/abs/1106.5182v1>.
- 1044 [46] ATLAS Collaboration, *ATLAS Luminosity Public Results*,
 1045 [https://twiki.cern.ch/twiki/bin/view/AtlasPublic/
 1046 LuminosityPublicResults#Multiple_Year_Collision_Plots](https://twiki.cern.ch/twiki/bin/view/AtlasPublic/LuminosityPublicResults#Multiple_Year_Collision_Plots).
- 1047 [47] ATLAS Collaboration, *ATLAS magnet system: Technical Design Report, 1*. Technical
 1048 Design Report ATLAS. CERN, Geneva, 1997.
- 1049 [48] ATLAS Collaboration, *ATLAS inner detector technical design report*, CERN/LHCC
 1050 (1997) 97–16.
- 1051 [49] G. e. a. Aad, *ATLAS pixel detector electronics and sensors*, J. Instrum. **3** (2008)
 1052 P07007.
- 1053 [50] ATLAS Collaboration, *ATLAS pixel detector electronics and sensors*, Journal of
 1054 Instrumentation **3** (2008) no. 07, P07007.
- 1055 [51] A. e. a. Abdesselam, *The barrel modules of the ATLAS semiconductor tracker*, .
- 1056 [52] A. Abdesselam and T. Akimoto, *The Barrel Modules of the ATLAS SemiConductor*
 1057 *Tracker*, Tech. Rep. ATL-INDET-PUB-2006-005. ATL-COM-INDET-2006-009.
 1058 CERN-ATL-COM-INDET-2006-009, CERN, Geneva, Jul, 2006.

- 1059 [53] A. Abdesselam and F. Anghinolfi, *The ATLAS semiconductor tracker end-cap module*,
 1060 Nucl. Instrum. Methods Phys. Res., A **575** (2007) no. 3, 353–389.
- 1061 [54] J. D. Jackson, *Classical Electrodynamics*. John Wiley & Sons, Inc., New Jersey, USA,
 1062 3 ed., 1991.
- 1063 [55] A. Bingl, *The ATLAS TRT and its Performance at LHC*, Journal of Physics:
 1064 Conference Series **347** (2012) no. 1, 012025.
- 1065 [56] ATLAS Collaboration, *The ATLAS TRT barrel detector*, Journal of Instrumentation **3**
 1066 (2008) no. 02, P02014.
- 1067 [57] ATLAS Collaboration, *The ATLAS TRT end-cap detectors*, Journal of
 1068 Instrumentation **3** (2008) no. 10, P10003.
- 1069 [58] R. Wigmans, *Calorimetry - Energy Measurement in Particle Physics*. Oxford
 1070 University Press, 2000.
- 1071 [59] ATLAS Collaboration, *ATLAS tile calorimeter: Technical design report*. CERN, 1996.
- 1072 [60] J. Proudfoot, *Hadron Calorimetry at the LHC*, .
- 1073 [61] B. A. et. al., *Construction, assembly and tests of the {ATLAS} electromagnetic barrel*
 1074 *calorimeter*, Nuclear Instruments and Methods in Physics Research Section A:
 1075 Accelerators, Spectrometers, Detectors and Associated Equipment **558** (2006) no. 2,
 1076 388 – 418.
- 1077 [62] A. E. L. A. E. C. G. et. al., *Construction, assembly and tests of the ATLAS*
 1078 *electromagnetic end-cap calorimeters*, Journal of Instrumentation **3** (2008) no. 06,
 1079 P06002.
- 1080 [63] M. A. et. al., *Construction and test of the first two sectors of the ATLAS barrel liquid*
 1081 *argon presampler*, Nuclear Instruments and Methods in Physics Research Section A:
 1082 Accelerators, Spectrometers, Detectors and Associated Equipment **479** (2002) no. 2-3,
 1083 316 – 333.
- 1084 [64] D. Green, *At the leading edge: the ATLAS and CMS LHC experiments*. World
 1085 Scientific, Singapore, 2010.

- 1086 [65] ATLAS Collaboration, *ATLAS detector and physics performance: Technical Design*
 1087 *Report, 1.* Technical Design Report ATLAS. CERN, Geneva, 1999. Electronic version
 1088 not available.
- 1089 [66] ATLAS Collaboration, *Expected performance of the ATLAS experiment-detector,*
 1090 *trigger and physics*, tech. rep., CERN, 2008.
- 1091 [67] T. Ferbel, *Experimental Techniques in High Energy Physics*. Addison-Wesley
 1092 Publishing Company, Inc., 1987.
- 1093 [68] T.Berger-Hryna and K. Nagano, *Trigger Menu Strategy for Run 2*, .
- 1094 [69] A. M. et al., *The ATLAS Data Acquisition and High Level Trigger system*, .
- 1095 [70] *Expected electron performance in the ATLAS experiment*, Tech. Rep.
 1096 ATL-PHYS-PUB-2011-006, CERN, Geneva, Apr, 2011.
- 1097 [71] E Gamma group, *Efficiency Measurements*, .
- 1098 [72] ATLAS Collaboration, *Electron reconstruction*, [https://twiki.cern.ch/twiki/bin/
 1099 viewauth/AtlasProtected/ElectronReconstruction](https://twiki.cern.ch/twiki/bin/viewauth/AtlasProtected/ElectronReconstruction).
- 1100 [73] *Preliminary results on the muon reconstruction efficiency, momentum resolution, and*
 1101 *momentum scale in ATLAS 2012 pp collision data*, Tech. Rep.
 1102 ATLAS-CONF-2013-088, CERN, Geneva, Aug, 2013.
- 1103 [74] ATLAS Collaboration, G. Aad et al., *Muon reconstruction performance of the ATLAS*
 1104 *detector in protonproton collision data at $\sqrt{s} = 13$ TeV*, Eur. Phys. J. **C76** (2016)
 1105 no. 5, 292, arXiv:1603.05598 [hep-ex].
- 1106 [75] M. Cacciari, G. Salam, and G. Soyez, *The anti- kt jet clustering algorithm*, Journal of
 1107 High Energy Physics **2008** (2008) no. 04, 063.
- 1108 [76] *Expected performance of the ATLAS b-tagging algorithms in Run-2*, Tech. Rep.
 1109 ATL-PHYS-PUB-2015-022, CERN, Geneva, Jul, 2015.
 1110 <http://cds.cern.ch/record/2037697>.
- 1111 [77] ATLAS Collaboration, *Performance of Missing Transverse Momentum Reconstruction*
 1112 *in Proton-Proton Collisions at 7 TeV with ATLAS*, Eur.Phys.J. **C72** (2012) 1844.

- 1113 [78] ATLAS Collaboration, *Top common object selection criteria*, <https://twiki.cern.ch/twiki/bin/viewauth/AtlasProtected/TopCommonObjects2011rel16>.
- 1115 [79] ATLAS Collaboration, *MissingEt calculation recommendation*,
 1116 https://twiki.cern.ch/twiki/bin/viewauth/AtlasProtected/TopETmissLiaison_EPS#Recommendations_for_Calculating.
- 1118 [80] ATLAS Collaboration, *Jet energy scale and its systematic uncertainty in proton-proton collisions at $\sqrt{s} = 7$ TeV in ATLAS 2010 data*, Tech. Rep.
 1119 ATLAS-CONF-2011-032, CERN, Geneva, Mar, 2011.
- 1121 [81] ATLAS Collaboration, *Jet energy measurement with the ATLAS detector in proton-proton collisions at $\sqrt{s} = 7$ TeV*, arXiv:1112.6426 [hep-ex]. submitted to
 1122 European Physical Journal C.
- 1124 [82] L. Moneta, K. Belasco, K. Cranmer, S. Kreiss, and M. Wolf, *The RooStats Project*,
 1125 arXiv:arXiv:1009.1003.
- 1126 [83] ATLAS Collaboration, *Jet uncertainties*, <https://twiki.cern.ch/twiki/bin/viewauth/AtlasProtected/JetUncertainties2011>.
- 1128 [84] ATLAS Collaboration, *Top systematic uncertainties*, <https://twiki.cern.ch/twiki/bin/view/AtlasProtected/TopSystematicUncertainties2011rel16>.
- 1130 [85] ATLAS Collaboration, *Jet Energy Scale uncertainty provider*, <https://twiki.cern.ch/twiki/bin/viewauth/AtlasProtected/JESUncertaintyProvider?rev=54>.
- 1132 [86] ATLAS Collaboration, *Jet Reconstruction Efficiency*, <https://twiki.cern.ch/twiki/bin/viewauth/AtlasProtected/TopJetReconstructionEfficiency>.
- 1134 [87] ATLAS Collaboration, *Energy Rescaler*,
 1135 <https://twiki.cern.ch/twiki/bin/viewauth/AtlasProtected/EnergyRescaler>.
- 1136 [88] ATLAS Collaboration, *Muon energy and momentum systematics*, <https://twiki.cern.ch/twiki/bin/viewauth/AtlasProtected/MCPAnalysisGuidelinesEPS2011>.
- 1138 [89] G. Cowan, K. Cranmer, E. Gross, and O. Vitells, *Asymptotic formulae for likelihood-based tests of new physics*, The European Physical Journal C-Particles and Fields **71** (2011) no. 2, 1–19.

- ₁₁₄₁ [90] ATLAS Collaboration, *Top Profiling Checks*, <https://twiki.cern.ch/twiki/bin/viewauth/AtlasProtected/TopProfilingChecks>.
- ₁₁₄₂
- ₁₁₄₃ [91] F. J. Massey, *The Kolmogorov-Smirnov Test for Goodness of Fit*, Journal of the
₁₁₄₄ American Statistical Association **46** (1951) no. 253, 68–78.
- ₁₁₄₅ [92] O. E. Barndorff-Nielsen and D. D. R. Cox, *Inference and asymptotics*, vol. 52.
₁₁₄₆ Chapman & Hall/CRC, 1994.
- ₁₁₄₇ [93] A. Caldwell, D. Kollar, and K. Kroninger, *BAT - The Bayesian Analysis Toolkit*,
₁₁₄₈ Comput. Phys. Commun. **180** (2009) 2197–2209, arXiv:0808.2552
₁₁₄₉ [physics.data-an].